Master thesis and internship[BR]- Master's thesis : Numerical Flutter Analysis of Flexible Wings: A Unified Cross-Sectional Properties, 3D Beam Modal Analysis, and SDPM Integration[BR]- Integration internship

Auteur : Abueltayef, Khader
Promoteur(s) : Andrianne, Thomas
Faculté : Faculté des Sciences appliquées
Diplôme : Master en ingénieur civil en aérospatiale, à finalité spécialisée en "aerospace engineering"
Année académique : 2024-2025
URI/URL : http://hdl.handle.net/2268.2/24830

UNIVERSITY OF LIÈGE - SCHOOL OF ENGINEERING

Numerical Flutter Analysis of Flexible Wings: A Unified Cross-Sectional Properties, 3D Beam Modal Analysis, and SDPM Integration

---

MASTER THESIS PRESENTED BY

ABUELTAYEF KHADER

IN ORDER TO OBTAIN THE DEGREE OF MASTER OF SCIENCE IN AEROSPACE ENGINEERING

THESIS SUPERVISOR

Professor **Thomas Andrianne**

University of Liège

JURY MEMBERS

Prof. Thomas Andrianne, Prof. DIMITRIADIS Grigorios, Prof. Xavier Amandolèse

Academic year 2024-2025

Abstract

A numerical framework for aeroelastic stability assessment of finite wings was developed by coupling a three-dimensional beam finite element structural model with an unsteady lifting-surface aerodynamic formulation provided by the `SDPMflut` software. Cross-sectional analyses supply spanwise distributions of area, bending and torsional rigidities, mass, and inertial properties, which are mapped to a beam mesh to assemble the undamped eigenvalue problem. A reduced modal basis is retained according to aeroelastic convergence criteria. Aerodynamic generalised forces are computed on a reduced-frequency grid and projected onto the structural modes to form the coupled frequency-domain problem.

For each airspeed, complex eigenvalues of the coupled system deliver modal frequencies and damping ratios. Flutter is identified from the zero crossing of modal damping, and the associated reduced frequency is recorded. Numerical credibility is established through two complementary procedures. First, a discretisation study demonstrates that the aeroelastic indicators are insensitive to further refinement beyond selected structural and aerodynamic resolutions. Second, a parameter-wise uncertainty analysis perturbs plausible aerodynamic and structural inputs around a nominal reconstruction and aggregates the resulting families of curves into envelopes. The dimensionless metric $\chi = f_h/f_\alpha$ succinctly characterises the relative placement of the first bending and torsional branches and explains trends in coalescence.

Validation on a ULiège wing configuration reconstructed from a high-fidelity dataset shows that the predicted modal patterns and the aeroelastic frequency– and damping– airspeed trends reproduce the expected behaviour, with flutter metrics consistent with reported experimental dispersion when equivalent modelling choices are adopted. The study indicates that structural properties govern frequency placement, whereas aerodynamic inputs primarily shape damping levels. The framework is fully reproducible, transparent in its data exchanges with the `SDPMflut` software, and readily extensible to additional configurations within the same modelling assumptions.

Keywords: aeroelasticity, flutter, finite wing, Timoshenko beam, 3D beam finite elements, cross-section properties, source–doublet panel method, `SDPMflut` software, modal analysis, flexion, torsion, coupling, sensitivity and convergence, damping.

Acknowledgement

Sincere gratitude is extended to **Professor Thomas Andrianne** of the University of ULiège for continuous guidance, constructive discussions, and the introduction of innovative ideas that shaped the direction of the research. Appreciation is also expressed for providing access to reference material on SDPM and for the steadfast support offered throughout regular meetings.

Deep appreciation is equally extended to **Professor Grigorios Dimitriadis** of the University of ULiège for his guidance and for granting access to the SDPMflut software and reference material on SDPM. The regular meetings and focused feedback significantly improved the clarity and rigour of the computational framework and its validation.

Enduring gratitude is owed to the parents, **Abueltayef Ahmed and Abueltayef Sireen**, for unwavering support, care, and encouragement from the earliest days of education to the completion of this thesis. A special acknowledgement is addressed to **Sireen** for constant encouragement and steadfast presence, which have been indispensable throughout demanding periods.

Warm thanks are conveyed to my sisters, **Hala, Alaa, and Sara**, for their understanding and support during intensive examination periods, project deadlines, and the sustained efforts required by this thesis.

Finally, appreciation is extended to my friend and colleague **Pirnay Maxime** for generous knowledge exchange and the sharing of wing-configuration datasets and related information, which facilitated consistent comparisons and strengthened the traceability of the numerical results.

Heartfelt appreciation is extended to everyone who played a role, both directly and indirectly, in this journey. Their support has been instrumental in realizing this accomplishment.

Contents

List of Figures

List of Tables

Chapter 1

Introduction

1.1 Context and motivation

Aeroelasticity is the multidisciplinary field that investigates the dynamic coupling among inertial, structural, and aerodynamic forces acting on a flexible body within a fluid flow. A classic representation for describing these couplings in aeroelasticity is Collar's triangle, introduced by Arthur Roderick Collar, as shown in Figure 1.1 . Classical bending–torsion flutter mechanisms and reduced-frequency effects are comprehensively documented in standard references [1], [2], [5].

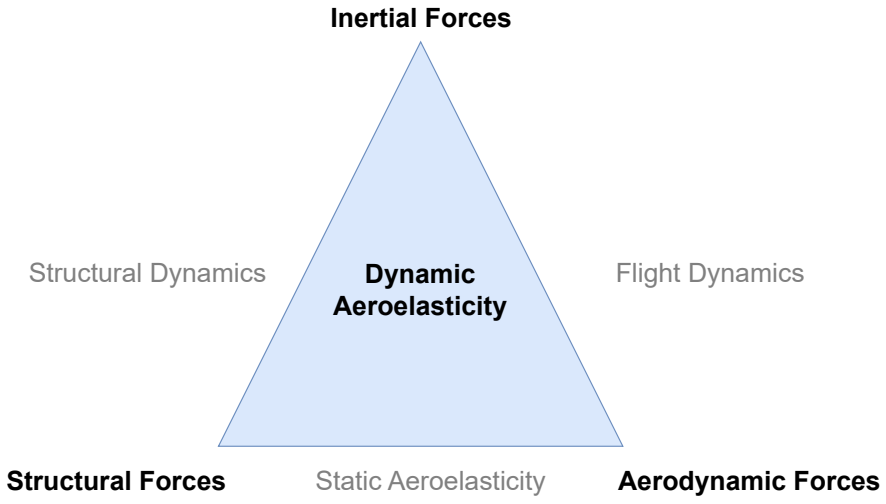

Figure 1.1: Collar's triangle illustrating the interaction of inertial, structural (elastic), and aerodynamic effects.

Aeroelastic phenomena have long been pivotal in aircraft design because they can lead to structural failure and impose significant limitations on the operational flight envelope [1]. In the scope of this thesis, attention is restricted to the analysis of **flutter** instabilities.

Flutter remains a critical instability in lifting surfaces and continues to constrain the preliminary design space of finite wings. The industrial development cycle increasingly demands early aeroelastic risk screening without recourse to costly instrumented wind-tunnel campaigns or simplified low-fidelity models. Under certain operational conditions, flutter can incite a dynamic instability where motion-induced aerodynamic forces transfer energy into the structure's natural modes of vibration. Therefore, the accurate prediction and comprehension of this behaviour are crucial for ensuring the stability and optimal performance of flexible systems across a wide range of engineering applications.

In experimental campaigns, flutter investigations typically require a dedicated wind-tunnel arrangement. The wing is instrumented with accelerometers or strain sensors, a calibrated excitation is applied, and modal parameters are identified at discrete airspeeds. Test matrices must cover angles of attack and speeds of interest while respecting structural limits and tunnel safety procedures. The process is resource-intensive, it demands careful rig design and calibration, and near-flutter operation entails strict risk mitigation. As a complement to such campaigns, a well-posed **numerical approach** can not only provide early guidance on discretisation choices, parameter sensitivities, and likely flutter trends **before** testing, but, additionally, it can support **post-test** interpretation through systematic comparisons [10], [9].

This thesis, therefore, focuses on wing configurations operating in subsonic compressible regimes, which are commonly encountered in applications such as solar-powered UAVs and slender wings. These structures are subject to considerable static and dynamic deformations, which brings into question the fidelity of traditional aeroelastic models in predicting the onset of flutter and their subsequent post-critical behaviour.

In the scope of this thesis, an advanced, fully numerical **computational framework** has been established to compute and deliver: (i) **structural** modal characteristics, (ii) a full set of **cross-sectional** properties with the necessary reference-point information, and (iii) **structural–aerodynamic coupling** data in the format required by the `SDPMflut` software. These outputs constitute the prerequisite inputs for linear **flutter** assessment of wing configurations. The lifting-surface formulation employed is consistent with classical unsteady-aerodynamics treatments for finite wings [2], [5].

1.2 Objectives of the thesis

The primary objective is to enable reliable prediction of flutter in modern flexible wings by establishing a robust numerical computational framework that supports early-stage design decisions and complements wind-tunnel campaigns through traceable and reproducible analyses with the `SDPMflut` software.

Accordingly, an advanced computational framework is established for linear flutter assessment of finite wings. The adopted modelling assumptions lie within the linear aeroelasticity framework for slender lifting surfaces [1], [2], [5]. Emphasis is placed on consistency of reference frames and units across modules, explicit metadata for intermediate and final results, and transparent input–output contracts.

The **structural** component relies on three-dimensional Timoshenko beam finite elements to compute wind-off natural frequencies and mode shapes for a spanwise line model placed on the elastic axis. Mode shapes are reconstructed at finite chordwise sampling points at each spanwise station to form a chordwise–spanwise grid suitable for aerodynamic coupling. Mass-normalised modes are retained, and the locations of the centre of gravity and the shear centre are tracked along the span to preserve physical consistency.

The **cross-sectional** component provides the spanwise distributions required by the beam formulation. Airfoil geometries are preprocessed to enforce trailing-edge closure and to represent skins and spars with piecewise-uniform materials. Mesh-based evaluation delivers A, EI_x, EI_z, GJ, J, centroid and shear-centre positions, as well as mass and rotary inertias per unit span. These fields are mapped to the structural mesh with continuity checks to avoid spurious stiffness or mass jumps.

The **aerodynamic** component employs a source–doublet panel method through the `SDPMflut` software to perform subsonic compressible unsteady analyses in the frequency domain. Generalised aerodynamic forces are computed on an appropriate reduced-frequency grid and projected onto the retained structural modes to form the coupled problem. Clear interfaces are maintained so that discretisation choices and solver options are documented and reproducible [3], [4].

Verification targets reproducibility and credible numerical behaviour. Discretisation and modal-truncation studies are conducted on a separate reference test case to determine mesh and basis sizes that render aeroelastic indicators insensitive to further refinement. Validation is then performed by comparison against experimental modal information reported for a ULiège laboratory wing, using only experimental points from the validated reference for comparison. No low-order Rayleigh–Ritz modelling and no experimental procedures are reproduced in the scope of this thesis [7].

Beyond these objectives, the computational framework is intended to provide early guidance on discretisation choices, parameter sensitivities, and likely flutter trends prior to testing, and to support post-test interpretation through structured comparisons with experimental outputs. Modelling assumptions can be calibrated transparently, robustness to structural-property uncertainty and damping can be assessed via envelopes, and regimes requiring refined measurements can be identified. The modular design and documented data exchange enable traceable, reproducible configurations and straightforward replication of case studies, facilitating informed design decisions and reducing iteration cost in subsequent experimental campaigns.

1.3 Thesis outline

The thesis is structured in four chapters. Chapter 1 introduces the context and motivation for numerical aeroelastic assessment of wings, states the objectives pursued in the scope of this thesis, and presents the overall organisation of the document.

Chapter 2 (**Methodology**) documents the numerical computational framework. The cross-section module is described with its geometry ingestion, meshing strategy, and spanwise property outputs. The structural modal module based on three-dimensional beam finite elements is presented with assembly steps, boundary conditions, eigen-solution, mass normalisation, and the construction of mode-shape fields on a chordwise–spanwise grid for aerodynamic coupling. The aerodynamic interface toward the SDPMflut software is specified, including coordinate conventions, data exchange, and solver configuration adopted for the analyses. Input and output tables are provided for each module. A separate reference test case is defined for discretisation and sensitivity studies, and recommended default settings are established from convergence evidence.

Chapter 3 (**Results**) reports numerical–experimental comparisons for a validated ULiège laboratory wing. Numerical models are rebuilt from geometry and material information, and results are compared against experimental points only. The influence of structural-parameter uncertainties is quantified, the effect of stiffness placement through the ratio f_h/f_α is analysed, and the impact of modal damping on flutter indicators is assessed. Figures and tables present frequency and damping trends with airspeed, the interaction of bending and torsional branches, and the robustness of predictions with respect to the modelling choices defined in Chapter 2.

Chapter 4 (**Conclusion and Perspectives**) summarises the main findings and the conditions under which they hold, identifies limitations related to modelling assumptions and numerical resolution, and outlines perspectives for extension, including possible improvements to cross-section modelling, mode-mapping strategies, and aerodynamic options within the `SDPMflut` software. The bibliography and appendices provide source references, export specifications, and auxiliary material required for reproducibility.

Chapter 2

Methodology

This chapter details the **computational framework** established for the numerical aeroelastic assessment of finite wings. The framework integrates a three-dimensional beam finite element structural model with an unsteady lifting-surface aerodynamic formulation through the `SDPMflut` software, and it delivers frequency– and damping– airspeed trends together with flutter metrics. The scope is purely numerical: all models, inputs, and outputs are defined, versioned, and processed within a reproducible computational environment.

The modelling strategy is driven by four principles. First, **traceability**: each intermediate quantity, from cross-sectional properties to modal bases and aerodynamic generalised forces, is saved with sufficient metadata to allow independent verification. Second, **consistency**: the same coordinate conventions, units, and sign definitions are enforced across the structural and aerodynamic modules. Third, **efficiency**: the structural representation is kept to a beam idealisation that captures the bending–torsion interplay governing classical flutter. Fourth, **robustness**: discretisation and solver tolerances are selected through systematic sensitivity studies, and envelope analyses are used to reflect plausible variability of inputs.

The structural module models the wing as a line-like Timoshenko beam with six degrees of freedom per node. Spanwise distributions of area, bending and torsional rigidities, mass, and radii of gyration are provided as inputs. The undamped eigenvalue problem is assembled and solved to obtain natural frequencies and mode shapes. Modal truncation is applied according to convergence of the aeroelastic response, and mass-normalised modes are retained to ensure a well-conditioned coupling with the aerodynamic forces. The mapping between geometric reference frames and analysis frames is made explicit, with the chordwise position of the centre of gravity and the shear centre tracked along the span.

The cross-sectional module delivers the spanwise property fields required by the beam model. The airfoil geometry is preprocessed to enforce trailing-edge closure, spars and skins are represented as piecewise uniform materials, and the resulting sections are meshed to compute geometric and warping quantities. The outputs comprise A, EI_x, EI_z, GJ, J, the locations of

the centroid and shear centre, and the mass and rotary inertias per unit span. These fields are interpolated on the structural mesh with continuity checks to avoid spurious stiffness jumps.

The aerodynamic module is based on the `SDPMflut` software, which provides a frequency-domain unsteady lifting-surface formulation. The lifting surface is discretised chordwise and spanwise, panel distributions are selected through a sensitivity study, and the reduced-frequency grid is chosen to cover the range relevant to the retained structural modes. Generalised aerodynamic forces are computed and projected onto the structural modal basis. Compressibility and Mach-number effects are treated as inputs of the aerodynamic solver and are varied when constructing uncertainty envelopes.

The aeroelastic coupling is formulated as a complex eigenvalue problem in the frequency domain. For each airspeed, the coupled matrices are assembled in modal coordinates, and the resulting complex eigenpairs deliver modal frequencies and damping ratios. Flutter is identified as the airspeed at which a damping curve crosses zero from negative to positive values, and the associated reduced frequency is reported. The full curves of frequency and damping versus airspeed are generated to visualise coalescence and separation of the bending and torsional branches.

To ensure credibility of the results, two complementary procedures are employed. A discretisation study quantifies the impact of structural mesh density and aerodynamic panelling on the aeroelastic predictions. In parallel, a parameter-wise uncertainty analysis perturbs selected aerodynamic and structural inputs around the nominal reconstruction and constructs envelopes of the frequency– and damping– airspeed curves. A compact frequency-placement metric, $\chi = f_h/f_\alpha$, is monitored to characterise how structural properties shift the relative position of the first bending and torsional branches.

The remainder of the chapter is organised as follows. The structural finite element module is presented in Section 2.1. The cross-sectional property module is described in Section 2.2. The aerodynamic formulation and its use through the `SDPMflut` software are summarised in Section 2.3. The flutter solution procedure is detailed in Section 2.4. An overview is provided in Section 2.5. Finally, Section 2.6 reports the discretisation and sensitivity analyses that underpin the numerical settings used in the results.

2.1 3D Beam Finite Element Structural Modelling

The structural dynamics of the wing are modelled using a three-dimensional finite element representation based on Timoshenko beam theory. This approach is chosen over the simpler Euler-Bernoulli theory as it accounts for transverse shear deformation, a phenomenon of significance in the analysis of modern aircraft wings, which are often constructed from advanced composite materials (multi-material) and may not always be considered slender. In the scope of this thesis, the wing's elastic axis is discretized into a series of interconnected beam elements, each representing a segment of the wing's span. This finite element model allows for the accurate computation of the wing's modal characteristics, including natural frequencies and mode shapes [5], [6], [10].

The formulation is designed to be particularly robust, accounting for configurations where the cross-section's centroid G, shear center C, and the elastic axis point E are not coincident. This capability is crucial for accurately capturing the bend-twist coupling inherent in complex airfoil geometries, an aspect that will be further detailed in Section 2.2.

2.1.1 Spatial Discretization

The structural analysis begins with the spatial discretization of the wing. The continuous elastic axis is represented by a finite number of nodes connected by beam elements, as illustrated in Figure 2.1. The continuous elastic axis of the wing is represented by a finite number of nodes connected by beam elements, as illustrated in Figure 2.1. The fidelity of this discretized model is dependent on the number of elements chosen. Non-structural components, such as engines or tip masses, can be included in the model as lumped masses added to the nodal degrees of freedom at their specific spanwise locations.

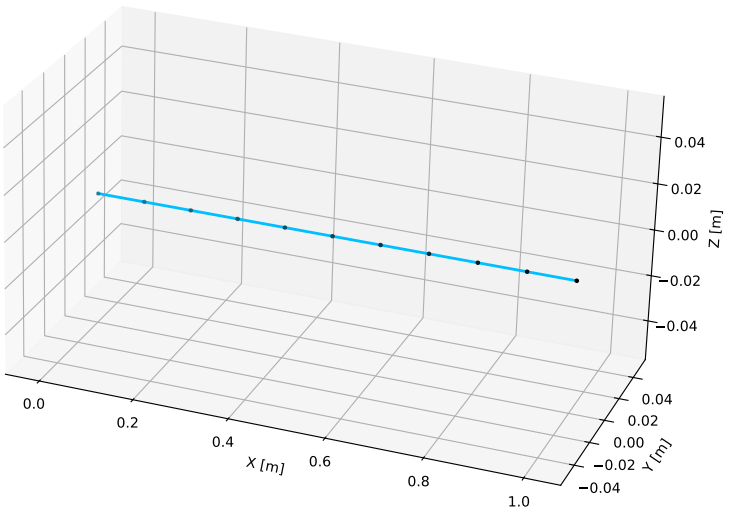

Figure 2.1: Discretization of the wing's elastic axis into nodes and 3D beam elements, showing the local coordinate system for an element.

2.1.2 3D Timoshenko Beam Element Formulation

Each element in the discretized model is a two-node Timoshenko beam element. The formulation requires the definition of both global and local reference frames to describe the element's kinematics and derive its properties.

The finite element formulation is comprehensive, accounting for axial deformation, biaxial bending (flapwise and lagwise) with transverse shear deformation in both planes, and torsion, including the effects of Saint-Venant warping. Furthermore, rotary inertia is retained, and a consistent mass matrix is assembled to accurately represent the element's inertial properties. For subsequent aeroelastic analysis, the computed mode shapes are mass-normalized to ensure a unit generalized mass.

A key feature of this advanced formulation is its ability to process section properties defined about multiple reference points, specifically the centroid, the shear center, and the elastic axis. This multi-reference approach ensures a high-fidelity capture of bending and torsion phenomena, particularly for complex airfoil configurations where these three points are not coincident.

Reference Systems

A global coordinate system, denoted as GCS (X, Y, Z), is used to define the overall geometry and orientation of the wing. In addition, each beam element has its own local coordinate system, ECS (x,y,z), with the x-axis aligned with the element's elastic axis, as shown in Figure 2.2. The transformation between the local and global systems is accomplished using a standard rotation matrix.

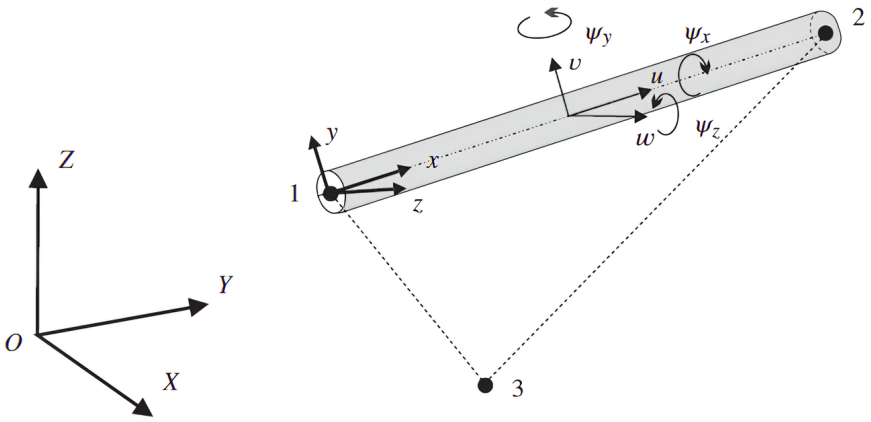

Figure 2.2: Three-dimensional beam element, illustrating the global and local coordinate systems and the nodal degrees of freedom, which include three translations ($u,\ v,\ w$) and three rotations ($\psi_x,\ \psi_y,\ \psi_z$).

Section Reference Points

Three main section reference points are defined, at every spanwise station, as:

- Centroid G used for translational and rotary inertia,
- Shear center C which defines the axis of pure Saint-Venant torsion,
- Elastic axis point E used to place the line model.

The cross-section module, as it will be shown in Section 2.2, provides the coordinates of G, C and E in $\{y, z\}$, in local axes, and the offsets $\vec{EG}$ and $\vec{EC}$. Additionally, cross-sectional properties are computed about multiple reference points, then transformed to the element frame so that bending inertias and stiffnesses about the elastic axis, the centroid, and the shear center are all available. Accurate knowledge of C is essential to capture bend–torsion coupling. In many Euler–Bernoulli-based workflows, common pre-processors do not provide C robustly, which forces indirect estimation and can degrade torsional fidelity.

Kinematics and Degrees of Freedom

Each node of the beam element possesses six degrees of freedom (DOFs): three translations along the local axes ($u,\ v,\ w$) and three rotations about these axes ($\psi_x,\ \psi_y,\ \psi_z$). Therefore, each element has a total of 12 DOFs. The displacement field within the element is interpolated from the nodal displacements using shape functions. Where, axial displacement and twist are interpolated linearly, and transverse displacements and rotations are interpolated with a field-consistent scheme that satisfies the shear-strain compatibility conditions, which prevents shear locking for thin sections and remains robust for thick sections.

Element matrices are integrated with Gauss–Legendre quadrature of sufficient order for stiffness and mass terms involving shear.

A key aspect of Timoshenko beam theory is that the rotations of the cross-section are treated as independent variables, which allows for the representation of shear deformation. The element degrees of freedom expressed in local axes:

$$q_e^T = [u_1 \ \ v_1 \ w_1 \ \ \psi_{x1} \ \ \psi_{y1} \ \ \psi_{z1} \quad u_2 \ \ v_2 \ \ w_2 \ \ \psi_{x2} \ \ \psi_{y2} \ \ \psi_{z2}] \ . \tag{2.1}$$

Indeed, Timoshenko kinematics allow the bending rotations to differ from the slopes of the transverse displacements, which introduces shear strains in the flapwise and lagwise directions through shear correction factors κ_y and κ_z, in local axes. This contrasts with Euler–Bernoulli elements where shear deformation is neglected and bending fields use cubic Hermite interpolation, a choice that is adequate only in slender limits and can under-predict coupling with torsion.

Elementary Mass and Stiffness Matrices

The kinetic and strain energies of the beam element are formulated based on the Timoshenko kinematic assumptions. Applying Hamilton's principle leads to the derivation of the element's consistent mass matrix, $\mathbf{M_e}$, and stiffness matrix, $\mathbf{K_e}$, in the local coordinate system. These 12×12 matrices encapsulate the inertial and elastic properties of the element, respectively. The formulation of these matrices, as implemented in the **computational framework**, is provided in Appendix A.1.

A key feature of Timoshenko beam theory is the decoupling of transverse displacements from the cross-sectional rotations. This allows for the definition of generalized strains that include transverse shear deformation. The axial strain (ε_x), bending curvatures (κ_y, κ_z), torsional twist rate (θ'_x), and transverse shear strains (γ_{xy}, γ_{xz}) along the element's local x-axis are defined as:

$$\varepsilon_x = \frac{\partial u_x}{\partial x} \, , \tag{2.2}$$

$$\kappa_y = \frac{\partial \theta_z}{\partial x}, \quad \kappa_z = -\frac{\partial \theta_y}{\partial x} \, , \tag{2.3}$$

$$\theta'_x = \frac{\partial \theta_x}{\partial x} \, , \tag{2.4}$$

$$\gamma_{xy} = \frac{\partial u_y}{\partial x} - \theta_z, \quad \gamma_{xz} = \frac{\partial u_z}{\partial x} + \theta_y \, . \tag{2.5}$$

The non-zero shear strain terms are what distinguish this formulation from the Euler-Bernoulli theory and enable a more accurate representation of the wing's flexibility.

2.1.3 Constitutive Relations and Sectional Properties

The relationship between the generalized stresses (internal forces and moments) and the generalized strains is defined by the constitutive matrix, $\mathbf{D}$. The vector of generalized stresses is given by $\boldsymbol{\sigma}^\top = [N, M_y, M_z, T, V_y, V_z]$, where N is the axial force, M_y and M_z are the bending moments, T is the torque, and V_y and V_z are the shear forces. The constitutive relationship is:

$$\boldsymbol{\sigma} = \mathbf{D} \, \boldsymbol{\epsilon} \, , \tag{2.6}$$

where $\boldsymbol{\epsilon}$ is the vector of generalized strains. The 6×6 constitutive matrix for an anisotropic material section is generally fully populated, but for materials with principal axes aligned with the local element axes, it simplifies to:

$$\mathbf{D} = \begin{bmatrix} EA & \cdot & \cdot & \cdot & \cdot & \cdot \\ \cdot & EI_y & EI_{yz} & \cdot & \cdot & \cdot \\ \cdot & EI_{yz} & EI_z & \cdot & \cdot & \cdot \\ \cdot & \cdot & \cdot & GJ & \cdot & \cdot \\ \cdot & \cdot & \cdot & \cdot & \kappa_y GA_{sy} & \cdot \\ \cdot & \cdot & \cdot & \cdot & \cdot & \kappa_z GA_{sz} \end{bmatrix} . \tag{2.7}$$

A significant feature of the implemented formulation is the retention of contributions from all significant deformation modes. These include axial stiffness (EA), biaxial bending stiffnesses (EI_y, EI_z), and the Saint-Venant torsional stiffness (GJ). Importantly, the formulation retains the cross-bending stiffness term (EI_{yz}) which accounts for bending coupling when the principal axes of the cross-section are not aligned with the local element axes $\{y, z\}$. In addition to the transverse shear stiffness terms ($\kappa_y GA_y$, $\kappa_z GA_z$).

Correspondingly, the consistent elemental mass matrix, $\mathbf{M}_e$, is formulated to account for both translational inertia, derived from the mass per unit length, and rotary inertia about the principal bending axes. To accommodate the continuous variation of properties along the wing's span, the sectional distributions are interpolated along the length of each element. The numerical integration required to derive these matrices is performed using Gauss-Legendre quadrature, with an order selected to be sufficient for an high-quality evaluation of all terms, including those arising from shear contributions.

2.1.4 Global System Assembly and Equations of Motion

The global mass and stiffness matrices for the entire wing structure, $\mathbf{M}$ and $\mathbf{K}$, are constructed by assembling the contributions from all individual elements. This process requires transforming each element's local matrices to the global coordinate system before summation.

The boundary conditions imposed on the finite element model are defined to replicate the physical constraints of the experimental test rigs used for the validation wings. This corresponds to a cantilevered configuration, featuring a fully clamped condition at the wing root and an unconstrained, free condition at the tip, unless an alternative setup is explicitly stated.

Once the global matrices are assembled, the undamped free vibration of the wing is governed by the generalized eigenvalue problem:

$$(\mathbf{K} - \omega^2 \mathbf{M})\, \boldsymbol{\phi} = \mathbf{0}\,, \tag{2.8}$$

where ω represents the **natural frequencies** and ϕ is the matrix containing the corresponding **mode shapes** (eigenvectors).

Equation 2.8 is solved with symmetric routines. Each eigenvector $\boldsymbol{\phi}_i$ is mass-normalised such that $\boldsymbol{\phi}_i^{\mathsf{T}} \mathbf{M}\, \boldsymbol{\phi}_i = 1$. Orthogonality checks $\boldsymbol{\phi}_i^{\mathsf{T}} \mathbf{M}\, \boldsymbol{\phi}_j = 0$ for $i \neq j$ are verified as a numerical quality control.

The solution of Equation 2.8 provides the fundamental dynamic characteristics of the wing, which are the essential inputs for the subsequent aeroelastic analysis.

2.1.5 Mode Shape Reconstruction for Aerodynamic Coupling

A critical final step in the structural analysis is the reconstruction of the one-dimensional beam mode shapes onto a two-dimensional chordwise–spanwise grid suitable for aerodynamic analysis. This process is necessary to interface the structural model with the panel-based grid of the `SDPMflut` software.

The reconstruction is performed for each mode shape individually. At every spanwise station corresponding to a finite element node, the translational and rotational degrees of freedom calculated for the elastic axis are used to define the motion of the entire cross-section at that station. This is achieved by applying rigid-section kinematics, where the airfoil section is assumed to translate and rotate as a rigid body. This kinematic expansion ensures that the relative contributions of bending and torsion are correctly projected from the elastic axis to all points on the airfoil chord.

Mathematical Formulation

The **translational** displacement vector $\mathbf{u}_p = [u_p,\ v_p,\ w_p]^T$ at any point p on the cross-section is determined from the translations at the elastic axis, $\mathbf{u}_{ea} = [u_{ea},\ v_{ea},\ w_{ea}]^T$, and the rotations of the section, $\boldsymbol{\phi} = [\phi_x,\ \phi_y,\ \phi_z]^T$. The position of point p relative to the elastic axis is given by the vector $\mathbf{r} = [r_x,\ r_y,\ r_z]^T$. The translational components of the mode shape field are thus given by the followings :

$$\Phi_x(p) = u_p = u_{ea} - r_z\phi_y + r_y\phi_z \ , \tag{2.9}$$

$$\Phi_y(p) = v_p = v_{ea} + r_z\phi_x - r_x\phi_z \ , \tag{2.10}$$

$$\Phi_z(p) = w_p = w_{ea} - r_y\phi_x + r_x\phi_y \ . \tag{2.11}$$

The rotational components of the mode shape field are derived from the spatial derivatives of the translational displacement field:

$$\Phi_{\phi_x} = \frac{\partial w}{\partial y} - \frac{\partial v}{\partial z} \ , \tag{2.12}$$

$$\Phi_{\phi_y} = \frac{\partial u}{\partial z} - \frac{\partial w}{\partial x} \ , \tag{2.13}$$

$$\Phi_{\phi_z} = \frac{\partial v}{\partial x} - \frac{\partial u}{\partial y} \ . \tag{2.14}$$

Simplification for Plate Mode Shapes

In the scope of this thesis, the structural models are based on plate-like wings, where the geometry is assumed to lie on the $z = 0$ plane. This simplification implies that any derivatives with respect to z are zero. Consequently, the equations for the rotational components of the mode shapes reduce to:

$$\Phi_{\phi_x} = \frac{\partial w}{\partial y} \,, \tag{2.15}$$

$$\Phi_{\phi_y} = -\frac{\partial w}{\partial x} \,, \tag{2.16}$$

$$\Phi_{\phi_z} = \frac{\partial v}{\partial x} - \frac{\partial u}{\partial y} \,. \tag{2.17}$$

The resulting six mode shape fields ($\Phi_x, \Phi_y, \Phi_z, \Phi_{\phi_x}, \Phi_{\phi_y}, \Phi_{\phi_z}$), defined over the complete two-dimensional grid, characterized by its structured arrangement of chordwise and spanwise nodes, are then exported into the specific `.mat` file structure required by the `SDPMflut` software. As it can be shown in Figure 2.3, for illustrative purposes only, an example of the deformed structural 2D grid for the first calculated mode shape, which represents the fundamental bending mode of the wing.

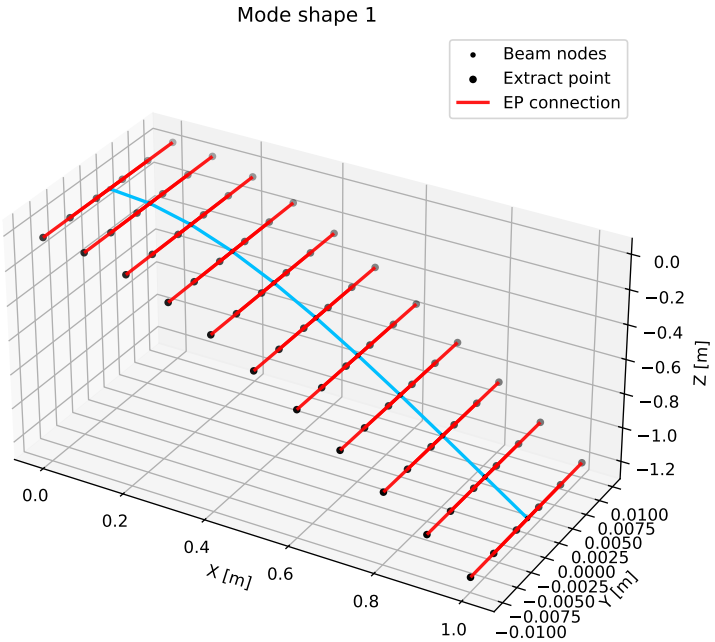

Figure 2.3: An illustration of the discretized 2D structural grid, characterized by its structured arrangement of chordwise and spanwise nodes, showing the deformation corresponding to the first mode shape. Shown in element's local coordinate system.

2.2 Cross-Sectional Property Modelling & Computation

The accuracy of the 3D beam finite element model, as detailed in Section 2.1, is fundamentally dependent on the precise calculation of the wing's cross-sectional properties at discrete points along its span. The `wingsecly` computational framework is equipped with a dedicated module to perform this critical task. This module serves as the foundational analysis stage of the entire computational framework, responsible for transforming a detailed geometric and material description of an airfoil's internal layout into a set of homogenized engineering properties. It is designed to analyze **complex, multi-material** airfoil cross-section configuration and its internal layout and compute a comprehensive set of geometric, inertial, torsional, and shear characteristics required for the advanced Timoshenko beam formulation. The successful execution of this module ensures that the subsequent 3D structural analysis is based on a high-fidelity representation of the wing's internal structure, thereby enabling an accurate prediction of its aeroelastic behaviour downstream, by `SDPMflut` software.

2.2.1 Principal & Concepts

The outputs from this module comprehensively define the geometry, stiffness, mass, torsion, and shear characteristics at discrete spanwise stations along the wing. A critical aspect of this analysis is the precise determination of three key reference points within the cross-section:

- The **centroid** (G), which represents the geometric center of the section. It serves as the reference point for computing the mass per unit length and the rotary inertias used in the element mass matrix.
- The **shear center** (C), which is the point in the cross-section through which transverse shear loads can be applied without inducing any torsional deformation. Its location is a function of the section's geometry and material distribution.
- The **elastic axis point** (E), which forms the locus of the shear centres along the wing's span. This axis is used to define the nodes of the 1D beam elements (the line model representing the wing) in the global structural model.

The accurate computation of the locations of these three points, and more importantly, the offsets between them (e.g., $\vec{EG}$ and $\vec{EC}$), is a prerequisite for a high-fidelity structural model. These offsets are directly responsible for capturing the critical bend-twist coupling phenomena inherent in asymmetric and complex airfoil configurations, which is a primary focus of the advanced Timoshenko beam formulation used in the scope of this thesis.

Consequently, once the locations of these three key reference points, the centroid, the shear center, and the elastic axis point, are determined, the computational framework proceeds to calculate the full spectrum of **geometrical and warping properties** required for the advanced

Timoshenko beam formulation, including the cross-sectional area, the mass per unit length derived from material densities, the second moments of inertia about various axes (including those about the centroid, the principal axes, and the modulus-weighted axes for composite sections), from which the bending rigidities are established, the Saint-Venant torsion constant and the warping function which together define the torsional rigidity, and finally, the effective shear areas and corresponding shear correction factors that characterize the section's response to transverse shear loads, and much more relevant properties.

The module can process a variety of wing, with internal layouts, configurations, from simple solid sections to more complex hollow, thin-walled profiles with multiple spars made of different materials, as will be illustrated, later on, in this thesis.

2.2.2 Geometry Modelling

The cross-section is represented by a set of interconnected parts with an explicit topology. This representation includes the outer airfoil skin with its spatially varying thickness, as well as the internal components such as spars, ribs, or webs, which are modelled as piecewise linear or curved entities. Additionally, the framework accommodates discrete reinforcements and fillers when they are present. The methodology is highly versatile, supporting any geometry type from common profiles like I-beams, rectangular, or circular beams, to any custom geometry, as long as the coordinates of its defining points are provided.

As illustrated in Figure 2.4, the two-dimensional representation of the cross-section provides a clear visualization of the interconnected components. The illustration delineates the outer airfoil skin and the internal structural elements, a rear and a forward spar, which are modelled as a set of interconnected linear and curved entities. Key features such as the definition of points and facets, as well as the identification of holes, are explicitly shown, confirming the topological precision of the model. This is only an illustrative example, where an airfoil type NACA 0015 was employed, and modelled as a thin-walled hollow airfoil, companied with two spars at different chordwise locations.

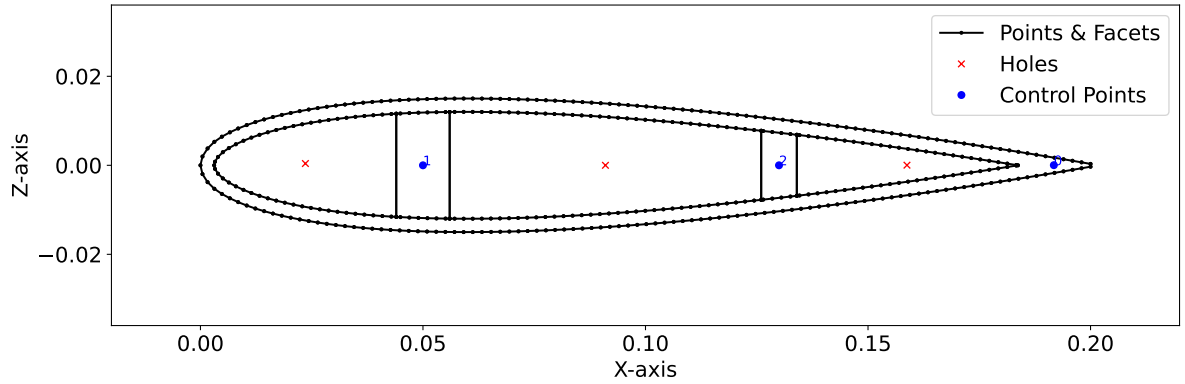

Figure 2.4: An illustration example of a two-dimensional geometric representation of a NACA 0015 airfoil cross-section. The illustration shows a thin-walled, hollow airfoil with a forward and a rear spar, delineating the outer skin and internal components. The mesh's topological precision is demonstrated through the explicit visualization of its defining points, facets, and holes.

2.2.3 Finite Element Meshing

To perform a numerical analysis of the cross-section, the constructed geometry must be discretized into a finite element mesh. The module employs a meshing algorithm to generate a high-quality mesh of triangular elements over the entire 2D domain, as shown in Figure 2.5. The mesh density is a controllable parameter, allowing for a trade-off between computational cost and the accuracy of the resulting properties.

The methodology is predicated on the generation of a two-dimensional manifold mesh for each station. This mesh is precisely defined to delineate both closed and open subdomains, and its topology is capable of accurately representing polygonal and curved boundaries. Consequently, this enables its application for cross-sectional integrals, as well as for Saint-Venant torsion and shear analyses.

As illustrated in Figure 2.5, the two-dimensional cross-section is discretized into a high-quality finite element mesh composed of triangular elements. The meshing algorithm employs an automated refinement strategy to increase element density at junctions and sharp edges. For this specific illustrative example, a uniform mesh size of 10^{-5} m was initially employed. However, the meshing algorithm automatically refines the connections between the spars and the thin-walled NACA 0015 airfoil. This targeted refinement ensures the accurate representation of complex geometric features and the precise capture of local stress concentrations, which will be useful for the internal computations to ensure a high-quality results of the cross sectional properties.

This visual representation not only confirms the successful discretization of the complex geometry but also illustrates the strategic distribution of elements and materials, with distinct regions allocated for different materials, such as aluminum and steel.

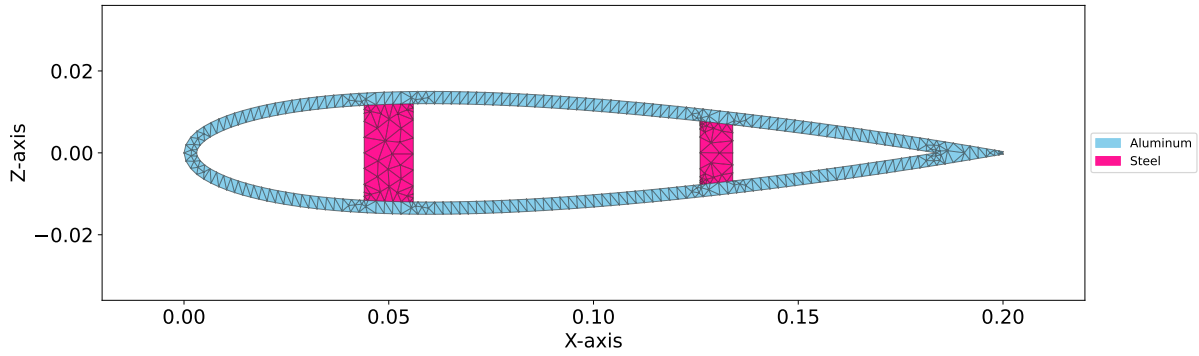

Figure 2.5: An illustration example of a finite element mesh of a NACA 0015 airfoil cross-section. The mesh is composed of high-quality triangular elements with a non-uniform distribution, as the meshing algorithm automatically refines the element size near critical junctions and sharp edges. It also illustrates the material allocation, with distinct regions assigned to aluminum and steel.

As illustrated in Figure 2.6, the computed cross-sectional properties reveal several key characteristics of the wing's internal structure. In this specific illustrative example, the elastic centroid and the elastic axis are observed to coincide. Furthermore, the figure delineates the shear center, which is distinct from the elastic centroid due to the non-trivial internal configuration of the wing. The complexity of the geometry and the heterogeneous material distribution necessitate a numerical approach for the determination of these properties, which cannot be obtained through manual calculation. The principal axes are also presented, providing a comprehensive representation of the section's inertial properties.

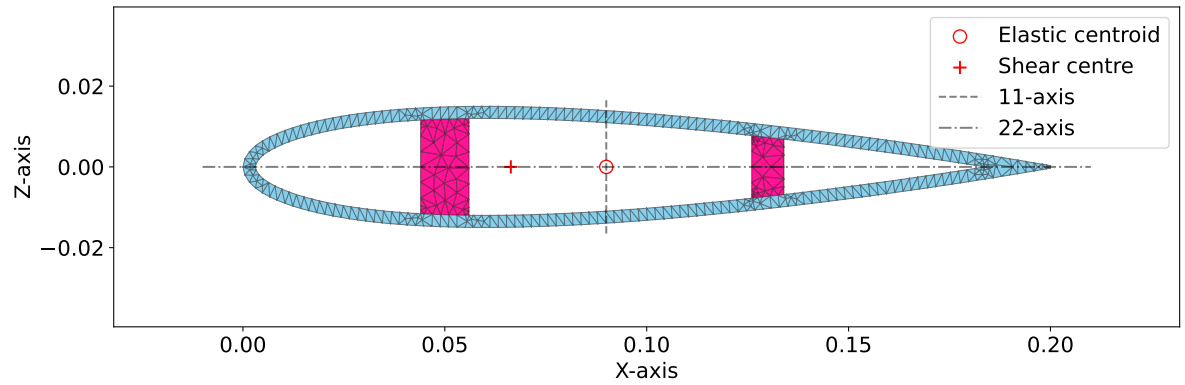

Figure 2.6: An illustration example of the computed cross-sectional properties for the NACA 0015 airfoil. The illustration depicts the location of the elastic centroid and elastic axis, which coincide for this symmetric section. It also shows the location of the shear center, which is distinct from the centroid due to the internal configuration of the wing. The principal axes are also presented.

The computational efficiency of the developed framework is a notable feature, as evidenced by the rapid execution time. The entire process, encompassing the translation of setup configurations, the generation of the final wing and airfoil geometries, the comprehensive computation of all geometrical and warping properties, and the subsequent visualization and local storage of the data, was successfully completed in a mere 1.564 seconds, for this illustrative example. This expedited performance demonstrates the framework's practical utility for conducting rapid and robust aeroelastic analyses.

2.2.4 Property Set Computation At Each Spanwise Station

With the meshed and materially-defined cross-section, a finite element analysis is conducted to determine its structural properties. This numerical analysis of the cross-section yields a comprehensive set of properties at each spanwise station, that are essential for populating the constitutive matrix ($\mathbf{D}$) of the Timoshenko beam elements. This includes the fundamental **geometric and inertial properties**, such as the cross-sectional area (A) and the coordinates of the centroid (G). Furthermore, the second moments of inertia about the local axes (I_{yy}, I_{zz}) and the product of inertia (I_{yz}) are computed with respect to the centroid. From these values, the principal second moments of inertia (I_1, I_2) and their corresponding principal rotation angle are determined. The framework also calculates the transformed second moments of inertia about the elastic axis (E) and the shear center (C) by employing exact transfer relations. In addition, the mass per unit length (m) and the rotary inertias about the centroid (I^G_{yy}, I^G_{zz}, I^G_{yz}) are established, taking into account the material densities.

Beyond the inertial characteristics, the analysis provides crucial **torsion and shear properties** (called sometimes warping properties). Specifically, the Saint-Venant torsion constant (J) is computed from the determined warping solution. The shear center (C) is then located based on the Saint-Venant shear flow resultants. Moreover, the effective shear areas (A_{sy} and A_{sz}), which are consistent with Timoshenko kinematics, are also derived. From these same shear-flow fields, the corresponding shear-correction factors (κ_y and κ_z) are obtained.

Finally, the framework provides essential **reference-point data**, which includes the coordinates of the elastic axis (E), the centroid (G), and the shear center (C) within the local coordinate system. This data also encompasses the offsets and transfer matrices required to accurately map stiffnesses and inertias between these key points.

The robust calculation of the shear center and the retention of the cross-bending stiffness term (EI_{yz}) are particularly important features. These properties allow the 3D beam model to accurately capture the bend-twist coupling effects that are critical for the flutter analysis of swept and composite wings. The direct computation of these advanced properties is a significant advantage over simpler methods that may neglect such couplings.

The two primary modules of the computational framework, the cross-section properties module and the 3D structural analysis module, are complementary and work in a dependent relationship. The 3D structural analysis module, which builds the wing configurations using 3D beam theory, calls upon the cross-section properties module to obtain the necessary geometric and warping properties. Upon successful computation, the cross-section properties module delivers the required results back, allowing the 3D structural analysis module to proceed with solving the eigenvalue problem and determining the modal characteristics, including natural frequencies and mode shapes.

2.2.5 Numerical Procedures

The numerical procedures employed in the analysis are designed to accurately determine the sectional properties of the wing. The initial step involves the computation of **section integrals**, which are performed on polygonal and curved subdomains to obtain fundamental properties such as the cross-sectional area (A) and the coordinates of the centroid (y_G, z_G), as well as the second moments of inertia about an arbitrary origin. The **transfer** of these properties to the centroid (G), and subsequently to the elastic axis (E) and the shear center (C), is executed through exact transfer relations. For composite or layered regions, these integrals are performed by integrating the **moduli and density** through the thickness.

The **Saint-Venant torsion** problem is subsequently solved on the section mesh under a unit twist rate to determine the warping function and its associated shear flow. The torsion constant (J) is derived from the energy expression. The shear center is located by iteratively adjusting the torque pole until the moment of the shear flow about the pole is null, thus ensuring its precise determination.

Finally, the **shear areas and correction factors** are calculated by solving two independent shear problems with unit transverse shear resultants in the y and z directions, we are always in the element's local coordinate system. The energy-equivalent effective shear areas (A_{sy} and A_{sz}) are extracted, and the corresponding shear-correction factors (κ_y and κ_z) are derived from the same shear-flow fields for use with the Timoshenko beam element. The **mass and rotary inertias** are also computed at each station. The mass per unit length (m) is derived from the subdomain densities and areas, while the rotary inertia tensor components about the centroid (G) are obtained from density-weighted second moments. Any discrete items, if present, are included as point-mass and point-inertia contributions.

2.2.6 Default Settings Used in the scope of this Thesis

Unless explicitly stated otherwise, the following default settings and procedures are adopted throughout this thesis. The meshing algorithm employs a curvature-based refinement strategy, with an enforced increase in mesh density near the leading and trailing edges as well as at all structural junctions. To ensure consistency across all analyses, a common finite element mesh is utilized for the Saint-Venant torsion and the two independent shear problems. Furthermore, the effective shear areas, A_{sy} and A_{sz}, are determined using an energy-equivalent extraction method. The location of the shear center is directly computed from the shear-flow resultants. All computed properties are transferred to the elastic axis (E) for seamless integration into the structural element formulation. Finally, the coordinates of the elastic axis (E), the centroid (G), and the shear center (C) are stored along with their respective offsets to facilitate subsequent aerodynamic mapping.

2.3 Aerodynamic & Aeroelastic Analysis (`SDPMflut`)

The aerodynamic and aeroelastic analysis in the present computational framework is performed by the `SDPMflut` software, developed by Prof. Dimitriadis [4], [3]. This software implements the compressible unsteady Source and Doublet Panel Method (SDPM) to model subsonic unsteady aerodynamics and to carry out aeroelastic stability studies. Its role in the computational framework is to provide the unsteady aerodynamic loads and the flutter solution once the structural modal data and the wing configuration have been defined.

In other words, `SDPMflut` does not handle modelling and computation of any structural models, but instead requires the structural modal characteristics as input in the form of modal matrices, finite element grid and mode shapes. This limitation is one of the main motivations for the development of the present computational framework, which automates the generation of the advanced structural modelling and cross-sectional properties computations and supplies them in the required format, `.mat` file format, as it was discussed earlier in the previous sections, Section 2.1 and Section 2.2.

2.3.1 Underlying Formulation

The `SDPMflut` software relies on the unsteady compressible potential-flow formulation of the source and doublet panel method. The governing equation is the linearised small-disturbance potential equation, which is solved under the **assumptions** of inviscid, irrotational, isentropic flow and small perturbations. A Prandtl–Glauert transformation, $\{\xi, \eta, \zeta\} = \{x/\beta, y, z\}$ with $\beta^2 = 1 - M_\infty^2$, is applied to account for compressibility effects.

Within these assumptions, the method provides efficient and accurate aerodynamic predictions for wings at subsonic Mach numbers, as long as the flow remains attached and free of shock waves. Additionally, the structural deformations are assumed small, so that the undeformed geometry is used as reference. These approximations render the method unsuitable for transonic cases, where shock-induced separation and the flutter dip cannot be captured.

The solution procedure consists of evaluating the unsteady surface potential, from which the perturbation velocities and the pressure distribution are obtained. The aerodynamic loads are then computed by integration over the wing surface. In the aeroelastic context, these loads are expressed in modal coordinates to form the generalized aerodynamic stiffness, damping and mass matrices, which are subsequently coupled to the structural modal equations.

2.3.2 Numerical Implementation and Discretisation

The aerodynamic discretisation employs a panel grid, characterized by m chordwise panels per side, n spanwise panels, and m_w wake panels. Panel numbering and optional non-uniform distributions are precisely defined. Specifically, there are m panels on both the lower and upper surfaces along the chord, with vertex numbering initiated at the lower trailing edge. An optional refinement strategy can be applied to increase panel density near the leading edge. Spanwise, the grid comprises $n/2$ panels per half-wing, with vertex numbering proceeding from the left tip to the right tip.

As it is illustrated in Figure 2.7, two chordwise panelling schemes of wings are presented, showing the panel numbering and distributions for both uniform and non-uniform cases. The grid consists of m panels on the lower surface and another m panels on the upper surface, for a total of $2m$ panels. The numbering of panel vertices starts with 1 at the lower trailing edge and proceeds upstream to the leading edge, which is vertex $m + 1$, before continuing downstream on the upper surface to vertex $2m + 1$ at the upper trailing edge.

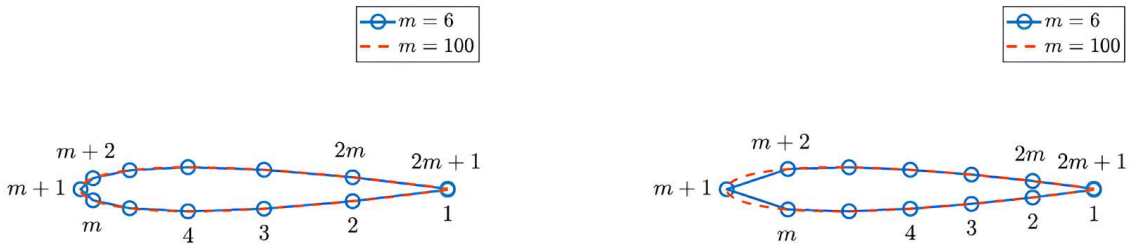

Figure 2.7: An illustration example of the chordwise panel numbering and distributions for both uniform (the right sub-figure) and non-uniform (the left sub-figure) cases.

As it is illustrated in Figure 2.8, the spanwise panelling scheme of wings is presented, showing the panel numbering and distributions for both uniform and non-uniform cases. The grid consists of $n/2$ panels on the left side and another $n/2$ panels on the right side, for a total of n panels and $n + 1$ panel vertices. The panel vertex numbering begins with 1 at the left wingtip and proceeds to the right, with the centerline at vertex $n/2+1$ and the right wingtip at vertex $n+1$.

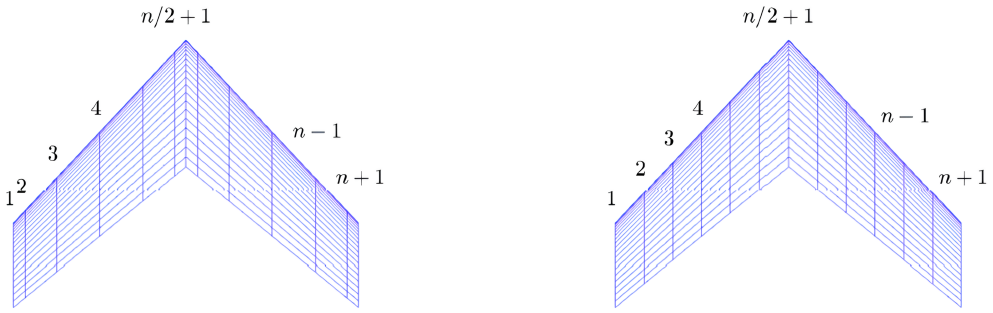

Figure 2.8: An illustration example of the spanwise panel numbering and distributions for both uniform (the right sub-figure) and non-uniform (the left sub-figure) cases.

It is important to note that the `SDPMflut` software adopts a coordinate system with the x-axis pointing downstream, the y-axis towards the right wingtip, and the z-axis upwards. Recalling that the global coordinate axes used for the computation framework developed in this thesis, are exactly the same, by convention, as the coordinate system of the `SDPMflut` software. The wake panels are consistently attached to the lower-surface trailing-edge segments and are convected downstream in the x-direction. This can be shown in Figure 2.9 .

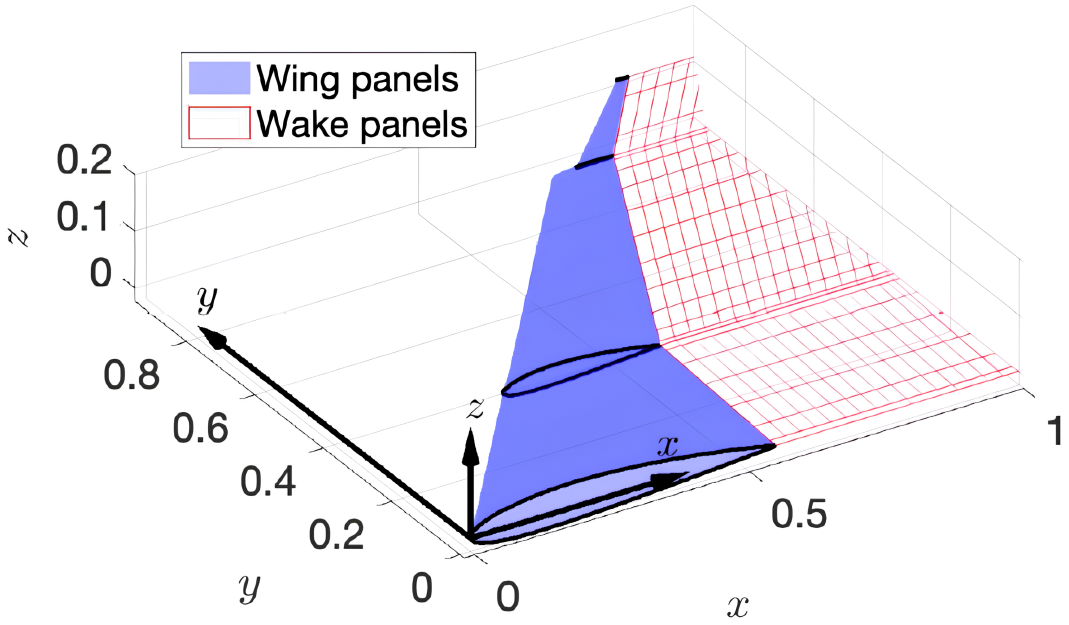

Figure 2.9: Coordinate system used by `SDPMflut` and by the computational framework developed in this thesis. The coordinate system, with the x-axis pointing downstream, the y-axis toward the right wingtip, and the z-axis upward, is adopted from the user guide for the `SDPMflut` software [4].

For robust interoperability and diagnostic purposes, the interface relies on the body-level arrays generated by the `SDPMflut` software. These arrays include the panel-vertex coordinates $(X_{p_0}, Y_{p_0}, Z_{p_0})$, the panel-centroid coordinates $(X_{c_0}, Y_{c_0}, Z_{c_0})$, and their flattened *all* vectors. The wake-vertex arrays $(X_{w_0}, Y_{w_0}, Z_{w_0})$ and the unit panel normals $(n_{x_0}, n_{y_0}, n_{z_0})$ are also utilized. These variables, which are constructed from the trapezoidal-section definitions, are subsequently used to perform consistency checks on coordinate systems and to verify interpolation bounds prior to the mode shape mapping procedure.

2.3.3 Structural Input and Mode Shape Mapping

The `SDPMflut` software requires the structural modal data to be provided through a dedicated `.mat` file, which must contain the **modal mass** ($\mathbf{A}$) and **stiffness** ($\mathbf{E}$) matrices, as well as the modal fields $\Phi_x, \Phi_y, \Phi_z, \Phi_\phi, \Phi_\theta, \Phi_\psi$. This modal basis is **mass-normalised**, resulting in the modal mass matrix $\mathbf{A}$ being a unit matrix ($\mathbf{A} = \mathbf{I}$) in modal coordinates, and the modal stiffness matrix $\mathbf{E}$ contains on its diagonal the values of the square of natural frequencies, such that $\mathbf{E} = \text{diag}(\omega_i^2)$. Additionally, a user-supplied array of structural damping ratios, $\boldsymbol{\zeta}_0$, is provided for each retained mode. The number of modes retained, K, is selected at run time.

The mode shapes obtained from the finite element spanwise line model, that were extended to a chordwise-spanwise 2D structural grid, are interpolated to the SDPM aerodynamic mean surface. This interpolation is specifically performed on the right half-wing camber surface via two-dimensional scattered-data cubic interpolation based on the (x, y) coordinates. The resulting modal fields are then mirrored across the $y = 0$ plane to the left half-wing, and identical deformations are applied to both the upper and lower surfaces. This procedure guarantees geometric compatibility, ensures symmetric mapping for cantilevered wings, and maintains an unambiguous orientation for the modal rotations.

2.3.4 Limitations & Integration Into The Computational Framework

While `SDPMflut` provides a robust and validated aerodynamic and aeroelastic solver, as previously stated, its scope is limited to the aerodynamic and aeroelastic computations. It does not include any pre-processing capabilities for **structural modelling**, **cross-sectional property calculation**, or finite element **structural discretisation**. The structural modal data must therefore be generated or delivered externally and imported as Matlab `.mat` files.

Furthermore, the aerodynamic formulation is restricted, by the **assumptions**, to subsonic attached flows, ignoring viscous and transonic effects, which can become significant at higher Mach numbers, but these latter limitations are out of the scope of this thesis.

To address the limitations about pre-processing capabilities, the present thesis develops complementary modules for structural and cross-sectional analysis. These modules automate the generation of the modal input data and enable a seamless coupling with `SDPMflut`. In this way, the complete computational framework provides an **end-to-end solution** for aeroelastic analysis, from geometry and structural modelling, cross-sectional geometrical and warping properties computations to flutter prediction.

2.3.5 Application within the Present Thesis

In the scope of this thesis, `SDPMflut` is used exclusively as the aerodynamic and flutter solver. The required input files containing the structural modal matrices and interpolated mode shapes are generated using the structural and cross-sectional modules described previously. The wing geometry and aerodynamic discretisation are defined through dedicated pre-processing scripts, ensuring consistency between the structural and aerodynamic models. The software is then employed to compute steady and unsteady pressure distributions, to evaluate generalized aerodynamic matrices, and to determine the flutter boundaries of the studied configurations.

2.4 Flutter Solution Procedure (via `SDPMflut`)

2.4.1 Aeroelastic Concepts

The present thesis is primarily focused on dynamic aeroelastic instabilities, particularly the phenomenon of flutter. Flutter is characterized as a self-excited, unstable structural oscillation that occurs at a specific frequency when energy is extracted from the airstream by the structure's motion. Beyond a critical airspeed, these oscillations can grow in amplitude, potentially leading to catastrophic structural failure. It is widely regarded as the most significant and challenging of all aeroelastic phenomena to predict.

As illustrated in Figure 2.10, a typical flutter case on an fundamental aeroelastic system with two modes of vibration. At wind-off conditions and below the flutter speed, the modes have well separated frequencies and positive damping ratios. As a result, the response of the system to non-zero initial conditions is a decaying oscillation (blue case: Stable). As the airspeed increases, the frequency gap between the modes decreases, the damping ratio of mode 1 increases and the damping ratio of mode 2 increases at first then decreases. When the airspeed coincides exactly with the system's linear flutter speed, the modal damping of mode 2 is exactly equal to zero (orange case: Neutrally Stable) and a constant amplitude oscillation can be observed. For any airspeed higher than that, the system features a negative damping ratio in mode 2 and a response amplitude that exponentially diverges as time passes is observed (red case:

Unstable).

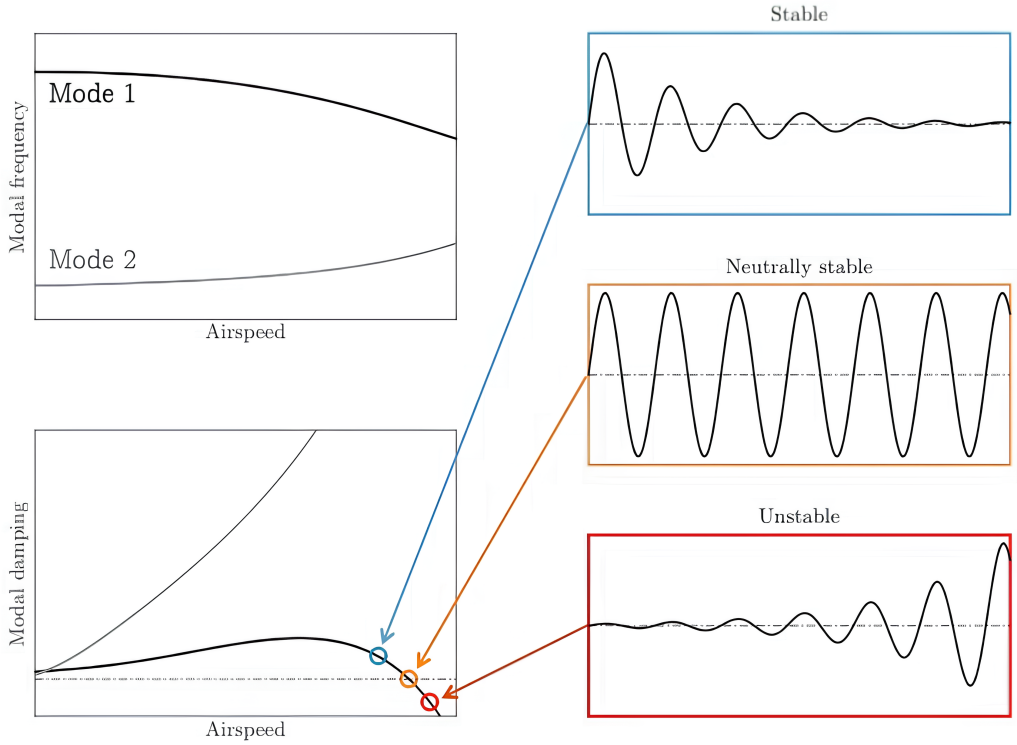

Figure 2.10: A typical flutter case for a two-mode aeroelastic system. The system's response to an initial disturbance is shown for three distinct cases: a stable, decaying oscillation below the flutter speed (blue case), a neutrally stable, constant-amplitude oscillation at the linear flutter speed (orange case), and an unstable, exponentially diverging oscillation above the flutter speed (red case).

In addition to identifying the onset of flutter, it is crucial to characterize the nature of the instability. As illustrated in Figure 2.11, flutter can manifest in different forms depending on the system's dynamic behaviour as it approaches and crosses the critical airspeed. In the case of *soft flutter*, the damping ratio decreases progressively with increasing airspeed until it crosses zero, resulting in a gradual onset of instability. In contrast, *hard flutter* is characterized by a sudden and abrupt decrease in damping, causing the system to transition abruptly from a stable to an unstable state.

Another notable scenario is the *hump mode*, where the modal damping initially decreases, crosses into an unstable regime (negative damping), and then increases again at even higher speeds, potentially restoring stability. In this case, flutter is confined to a limited range of velocities, which can make its detection and analysis more complex. These different behaviours are illustrated in Figure 2.11.

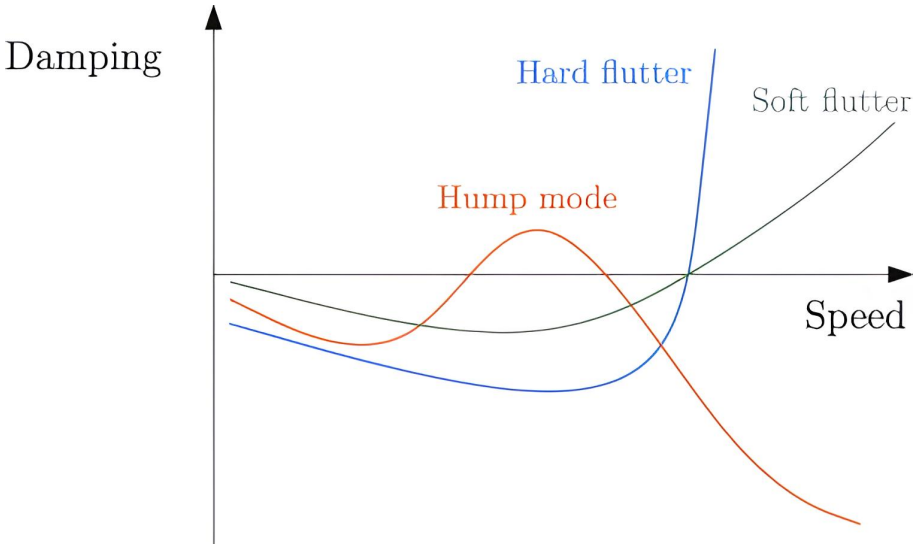

Figure 2.11: Different types of flutter instabilities. The figure illustrates three distinct scenarios: *soft flutter*, characterized by a gradual decrease in damping, *hard flutter*, showing an abrupt and sudden drop in damping, and a *hump mode*, where the system enters and then exits an unstable regime as airspeed increases.

2.4.2 Aeroelastic Equation of Motion

The primary objective of a flutter analysis is to determine the critical flight speed at which a structure's aeroelastic damping vanishes, leading to an oscillatory instability. This phenomenon is governed by the coupled aeroelastic equation of motion in the modal domain, which can be expressed in its general form as:

$$\mathbf{A}\ddot{\mathbf{q}} + \mathbf{C}\dot{\mathbf{q}} + \mathbf{E}\mathbf{q} = \mathbf{F}_{\text{aero}}(\mathbf{q}, \dot{\mathbf{q}}, \dots) \ ,$$

where, $\mathbf{A}$, $\mathbf{C}$, and $\mathbf{E}$ represent the structural modal mass, damping, and stiffness matrices, respectively, while $\mathbf{q}$ is the vector of generalised coordinates. The right-hand side, $\mathbf{F}_{\text{aero}}$, represents the generalised unsteady aerodynamic forces, which are a function of the modal displacements, velocities, and accelerations. These forces are typically computed for a range of reduced frequencies, k, and Mach numbers, M_∞.

The solution to this problem is an eigenvalue search for a complex frequency, $\lambda = \sigma + i\omega$, where a positive real part ($\sigma > 0$) signifies instability, and a zero real part ($\sigma = 0$) identifies the flutter boundary. The `SDPMflut` software, as described in Section 2.3, provides a robust implementation of this analysis, which is central to this thesis.

2.4.3 Flutter via `SDPMflut` Software

This section specifies how flutter indicators are obtained using the `SDPMflut` software once the structural modes and the aerodynamic mapping have been prepared. The procedure defines the reduced-frequency sampling, the assembly of generalised aerodynamic matrices, the determinant iteration over airspeed, and the detection and refinement of flutter conditions. Configuration choices and quality checks are stated to ensure traceable, reproducible analyses.

Generalised Aerodynamic Forces and Flutter Solution

For each reduced frequency k, the `SDPMflut` software assembles the generalised aerodynamic matrices, $\mathbf{Q}_0(k)$, $\mathbf{Q}_1(k)$, and $\mathbf{Q}_2(k)$. The coupled aeroelastic eigenproblem is subsequently solved using a determinant-iteration method at discrete airspeeds, Q_∞. This procedure seeks the reduced complex eigenvalue,

$$p = g + ik \ ,$$

that makes the determinant of the quadratic pencil vanish. With, g represents the reduced damping, and k is the reduced frequency.

The matrices $\mathbf{Q}_j(k)$ are precomputed at selected k values and interpolated during the iteration to reduce computational cost while preserving accuracy. The system's stability is continuously monitored through the modal damping ratio,

$$\zeta_i(Q_\infty) = -\Re(\lambda_i)/|\lambda_i| \ .$$

A sign change in ζ_i indicates instability and triggers a refined determinant iteration to precisely locate the **flutter** airspeed, Q_F, and the corresponding **flutter** reduced frequency, k_F, which define the critical flutter condition.

2.5 Overview of the Computational Framework

The computational framework developed in the scope of this thesis has been designed to establish a complete and automated numerical chain for the aeroelastic analysis of wings. It integrates **structural modelling**, **cross-sectional property computation**, **Aerodynamic & Aeroelastic Analysis (using `SDPMflut`)**, and **flutter prediction** into a unified process. Each of the individual modules presented in Sections 2.1–2.4 is connected in a **sequential** manner, ensuring that the outputs of one stage constitute the inputs of the subsequent stage. The framework is structured to provide a rigorous and consistent transition from the detailed description of a **wing configuration** to the determination of its **aeroelastic** stability boundaries.

The process initiates, internally, with the **cross-sectional property module**, which transforms the **geometrical and material description** of the wing's airfoil into homogenized engineering properties. These properties include the stiffness, inertia, shear and torsional constants, and the precise locations of the centroid, shear center, and elastic axis. The computed sectional data, evaluated at discrete **spanwise stations**, forms the foundation for the next stage.

The **structural finite element module** then discretizes the wing's elastic axis into a series of **Timoshenko** beam elements, each **assigned** the cross-sectional properties provided by the previous stage. This step produces the **modal characteristics** of the structure, namely **natural frequencies and mode shapes**, which are **mass-normalized** to be compatible with the **Aerodynamic & Aeroelastic Analysis (using `SDPMflut`)**. Non-structural masses or external components can also be incorporated at this stage, further refining the dynamic model of the wing.

Once the structural model is established, the **Aerodynamic & Aeroelastic Analysis** based on the `SDPMflut` software is employed. This component models the unsteady aerodynamic loads using a source and doublet panel method and expresses them in modal coordinates consistent with the structural formulation. The aerodynamic discretization of the lifting surface is defined in terms of chordwise and spanwise panel distributions, enabling the accurate capture of **unsteady aerodynamic effects** in the **subsonic** regime.

Finally, the **flutter solution module** integrates the structural modal data with the generalized aerodynamic forces provided by `SDPMflut`. Through this coupling, the aeroelastic eigenvalue problem is solved, and the **flutter boundary** is determined. The procedure identifies not only the critical speed at which instability occurs but also the type and nature of the instability, which can be determined by inspection, whether of soft, hard, or hump mode character.

In summary, the **computational framework** enables a systematic and high-fidelity aeroelastic analysis by combining advanced structural modelling, precise cross-sectional characterization, and efficient aerodynamic and aeroelastic analysis (using `SDPMflut` software). The schematic

workflow presented in Figure 2.12 illustrates the sequence of modules and the data transfer between them, highlighting the integration of the complete process from the wing definition to the final flutter prediction.

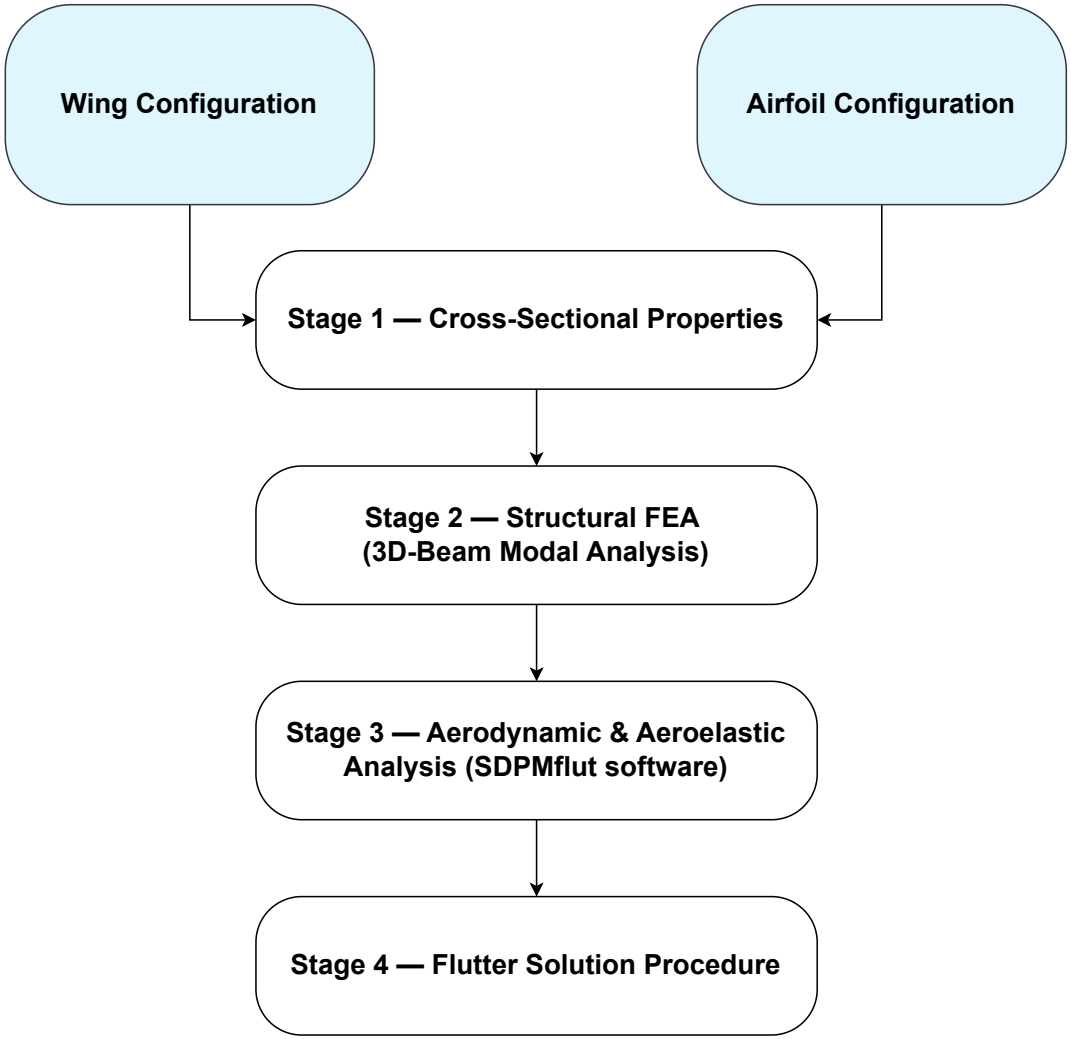

Figure 2.12: Overview of the developed computational framework for aeroelastic analysis. The process integrates wing and airfoil configuration inputs with four sequential modules: cross-sectional property computation, structural finite element modelling, aerodynamic coupling via `SDPMflut`, and flutter solution.

In order to provide a clear overview of the developed computational framework, the main inputs, core computations, and outputs of each constituent block are systematically summarized. The Wing Configuration and Airfoil Configuration are first introduced as the fundamental definitions of the problem, after which the four sequential stages of the framework are presented. For clarity and conciseness, each block is reported in the form of a representative table, which highlights its role within the overall process and its connection to the subsequent stages. These tables are reported in Table 2.1, Table 2.2, Table 2.3, Table 2.4, Table 2.5 and Table 2.6 .

Table 2.1: Wing Configuration definition. This block establishes the global structural and aerodynamic discretization of the wing and provides all platform and boundary information required to initialize the subsequent modules.

Inputs	• Span b, root chord c_r, tip chord c_t, taper ratio λ • Reference lines $x_{\mathrm{LE}}(y)$ and $x_{\mathrm{TE}}(y)$ • Boundary conditions • Discretizations n_{spanwise}, $n^{\mathrm{aero}}_{\text{spanwise}}$, $n^{\mathrm{aero}}_{\text{chordwise}}$ • Number of retained modes n_{modes} • Lumped masses $(y_i, r_x, r_y, r_z, m, I)$ if any • Air density ρ • Speed grid $\{U_j\}$
Utility	• Structural nodes and connectivity of the elastic axis • Aerodynamic panelling parameters • Global reference frames for the aeroelastic model

Table 2.2: Airfoil Configuration definition. This block specifies the sectional layout and material composition, which are fundamental for generating accurate sectional properties.

Inputs	• Material properties $(E, \nu, \rho_s, \sigma_y)$ with identification attributes • Airfoil `.dat` (or `.txt`) path • Construction type: solid filled, thin-walled hollow, or thin-walled with spars • Spar definitions $(x/c, t_{\text{spar}}, \text{material})$
Utility	• Cleaned two-dimensional cross-sectional geometries per span station • Meshed layouts of skins, spars, and caps with material tags • Prepared dataset for advanced sectional property computation

Table 2.3: Stage 1 – Cross-Sectional Properties Module. The module produces an advanced and comprehensive set of sectional characteristics, extending beyond basic geometry, indispensable for high-fidelity structural and aeroelastic modelling.

Inputs	• Two-dimensional airfoil meshes and material tags (from Airfoil Config.) • Spanwise stations (from Wing Config.)
Core computations	• EA (axial rigidity) • EI_{xx}, EI_{yy}, EI_{xy} (bending rigidities about multiple references) • GJ (torsional rigidity), J (Saint-Venant torsion constant) • E_{eff}, G_{eff}, ν_{eff} (effective composite moduli) • A_{sx}, A_{sy} (shear areas), κ_x, κ_y (shear correction factors) • I_{xx}, I_{yy}, I_{xy} (inertias), A (area) • Determination of centroid (x_G, y_G), shear center (x_S, y_S), elastic axis, and frames
Outputs	• Spanwise distributions of the complete property set • Reference points and offsets for integration into the beam model

Table 2.4: Stage 2 – Structural Finite Element Analysis. This stage provides a refined static and dynamic representation of the wing based on an advanced Timoshenko beam formulation, capable of solving static loads, damped and undamped modal problems.

Inputs	• Sectional properties from Stage 1 • Elastic axis mesh (from Wing Config.) • Boundary conditions • Lumped masses • Number of retained modes n_{modes}
Core computations	• Assembly of 3D Timoshenko beam stiffness, mass, and damping matrices • Static solver: $\mathbf{Ku} = \mathbf{F}$ for displacements under applied loads • Undamped eigenvalue problem: $(\mathbf{K} - \omega^2\mathbf{M})\ \boldsymbol{\phi} = 0$ • Damped eigenvalue problem: $(\mathbf{K} + j\omega\mathbf{C} - \omega^2\mathbf{M})\ \boldsymbol{\phi} = 0$ • Inclusion of shear deformation, rotary inertia, Saint-Venant warping, and offsets to centroid, shear center, and elastic axis • Mass normalization and modal truncation
Outputs	• Modal characteristics $\{\omega_r, \boldsymbol{\phi}_r(y)\}$ for undamped and damped cases • Mass-normalized mode shapes with mapping to aerodynamic grid • Structural export files for aeroelastic coupling

Table 2.5: Stage 3 – Aerodynamic & Aeroelastic Analysis using `SDPMflut`. This stage delivers unsteady aerodynamic operators in modal coordinates, forming the link between structural dynamics and aeroelastic stability.

Inputs	• Modal basis and mapping (from Stage 2) • Aerodynamic panel discretization (from Wing Config.) • Air density ρ • Speed grid $\{U_j\}$
Core computations	• Source and doublet panel method for subsonic unsteady flow • Evaluation of pressure distributions and aerodynamic loads • Projection of loads into the modal subspace
Outputs	• Generalized aerodynamic operators $\mathbf{Q}(k)$ vs. reduced frequency or airspeed • Equivalent state-space representation compatible with modal equations

Table 2.6: Stage 4 – Flutter Solution Procedure. This final stage solves the coupled aeroelastic eigenproblem to identify the onset of instability and to characterize the flutter.

Inputs	• Modal stiffness and mass matrices (from Stage 2) • Generalized aerodynamic forces (from Stage 3) • Air density ρ • Speed or Mach sweep $\{U_j\}$
Core computations	• Solution of the aeroelastic eigenvalue problem • Tracking of eigenvalues with speed • Identification of damping evolution and instabilities
Outputs	• Critical flutter speed U_f and the corresponding flutter reduced frequency, k_F • Natural frequency versus airspeed curves for retained modes • Damping versus airspeed curves for retained modes

2.6 Parameter & Sensitivity Study on a Reference Test Case

2.6.1 Reference Test Case

All sensitivity studies reported in this chapter are performed on a single reference wing section, built from the publicly available NACA 0015 dataset and modelled as a solid filled cross-section in Aluminum. Unless explicitly stated otherwise in each subsection, the same material definition, geometry, and boundary conditions are used.

Definition and baseline settings

- **Airfoil and construction** : NACA 0015, solid filled cross-section,
- **Preprocessing** : trailing-edge closure applied to raw `.dat` coordinates, then resampled to $n = 200$ uniformly distributed points along the contour,
- **Material** : Aluminum with $E = 70\,\text{GPa}$, $\nu = 0.33$, $\rho = 2700\,\text{kg m}^{-3}$,
- **Geometry** : chord $c = 0.20\,\text{m}$, span segment $b = 1.0\,\text{m}$ for the structural beam,
- **Coordinate frame** : x along chord, y along span, z out-of-plane; the elastic axis is placed along the y-axis,
- **Boundary conditions** : root clamp at $y = 0$, free tip at $y = b$,
- **Discretizations for this chapter** : structural mesh as specified in each sweep, aerodynamic panelling defined in the corresponding subsection, modal truncation per test,
- **Lumped masses** : none unless stated otherwise.

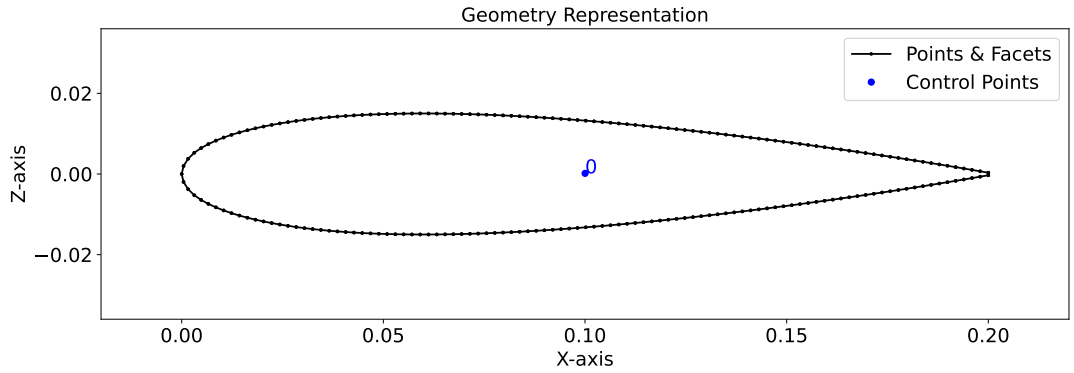

Figure 2.13: Geometric representation of the reference airfoil section used throughout the sensitivity study. Control points and facets are shown for the NACA 0015 geometry after preprocessing and trailing-edge closure. The airfoil contour is resampled to $n = 200$ uniformly distributed points.

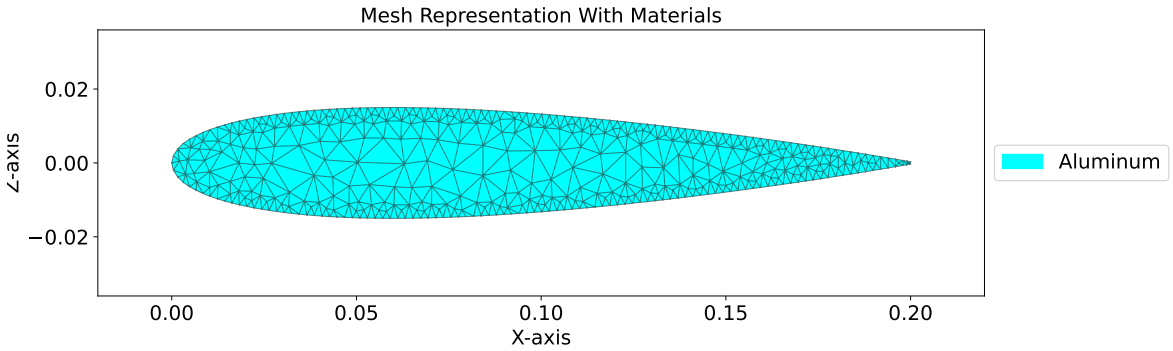

Figure 2.14: Material tagging for the meshed cross-section of the reference case. The example shows a homogeneous aluminum layout consistent with the material definition adopted in this chapter.

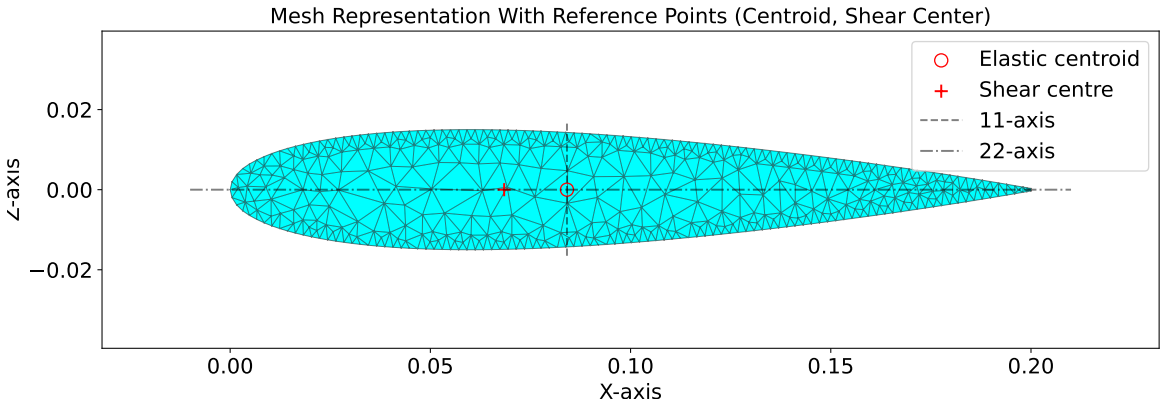

Figure 2.15: Finite-element mesh of the reference section with key reference points and axes. The elastic centroid and the shear center are indicated together with the local section axes used to assemble the beam model.

2.6.2 Airfoil Preprocessing Robustness

Before addressing the influence of discretization parameters on the aeroelastic solution, the robustness of the airfoil preprocessing stage is first examined. Figures 2.16 and 2.17 illustrate two essential corrections applied to the input airfoil coordinates, namely trailing-edge closure and uniform resampling. For this illustration, the NACA 0015 `.dat` file has been used.

As shown in Figure 2.16, the raw coordinates obtained from the `.dat` file present a trailing-edge gap of approximately 0.63 mm. Such an open contour is unsuitable for the computation of sectional properties, since it leads to spurious values of torsional and shear constants. The implemented routine ensures watertight closure of the contour while preserving the global geometry.

In Figure 2.17, the point spacing distribution along the raw contour is compared to that of the uniformly resampled geometry. The raw coordinates exhibit strong variability in spacing, with a coefficient of variation of nearly 53%. After resampling to $n = 200$ points, the coefficient of variation is reduced to 5%, yielding a contour with homogeneous resolution. This uniform discretization is crucial for the stability of the finite element meshing and for the accurate evaluation of high-order sectional properties such as warping functions and shear correction factors.

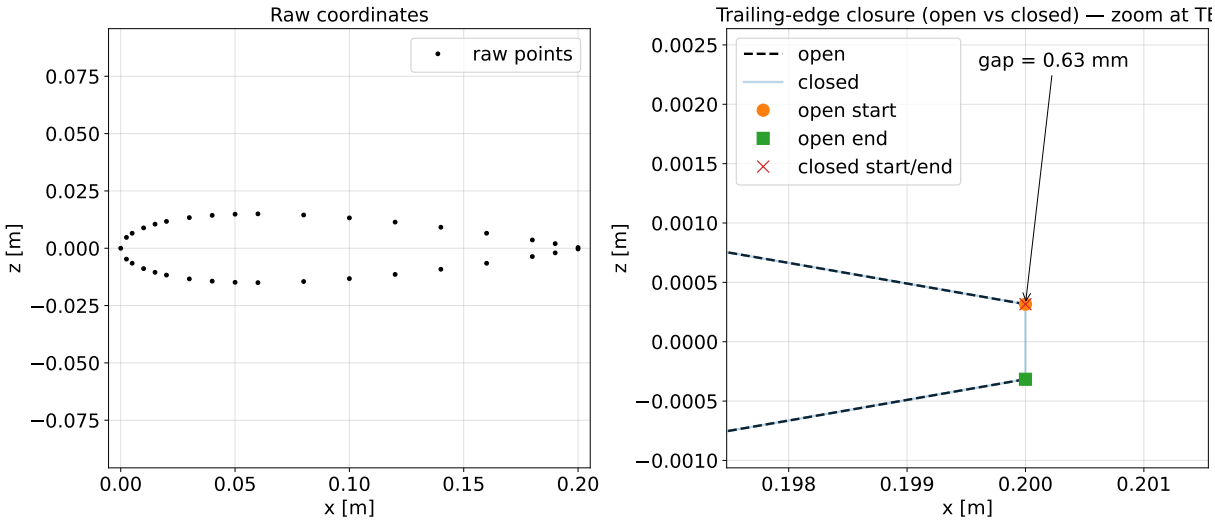

Figure 2.16: Raw coordinates of the NACA 0015 airfoil and trailing-edge closure. Left: raw coordinates showing the open trailing edge. Right: zoom at the trailing edge highlighting the gap of 0.63 mm between the open contour and the closed watertight contour.

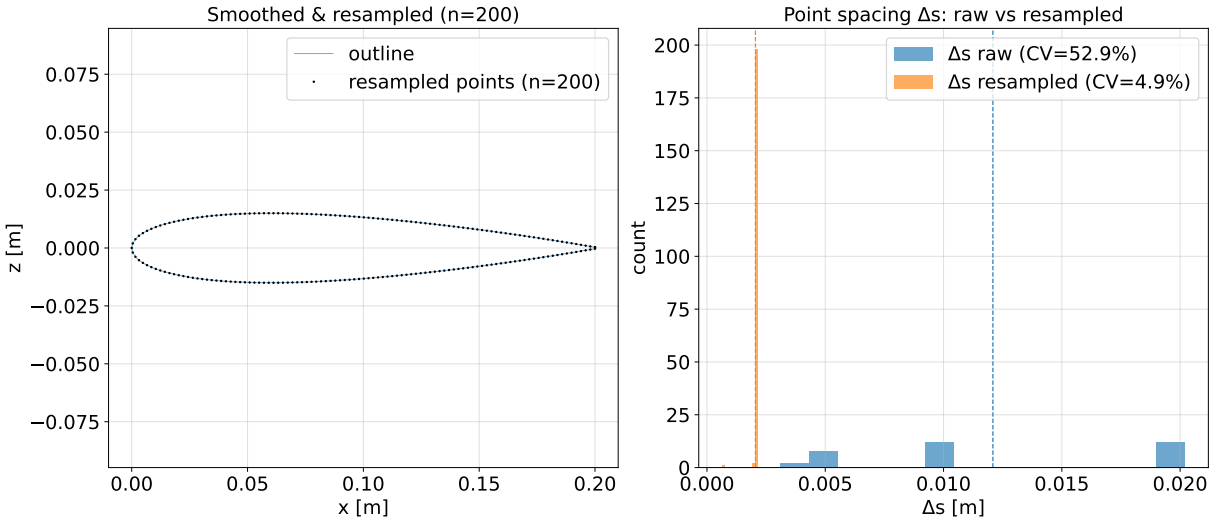

Figure 2.17: Smoothed and resampled representation of the NACA 0015 airfoil. Left: contour resampled to $n = 200$ uniformly distributed points. Right: histogram of point spacing Δs comparing raw coordinates (CV $= 52.9\%$) with the resampled contour (CV $= 4.9\%$), demonstrating the improved uniformity.

2.6.3 Structural Discretization Sensitivity

The accuracy of the finite element beam model is directly influenced by the number of spanwise stations used to discretize the elastic axis. If the number of elements is too small, the computed modal frequencies and mode shapes may be significantly distorted. On the other hand, an excessively fine discretization increases computational cost without providing additional accuracy for the first few structural modes, which are the most relevant for aeroelastic analysis.

In this subsection, the sensitivity of the computed modal characteristics to the number of spanwise stations is investigated. A convergence study is performed by systematically increasing n_{spanwise}, and the resulting natural frequencies and mode shapes are compared. The objective is to determine the discretization level at which the structural modal solution becomes mesh-independent.

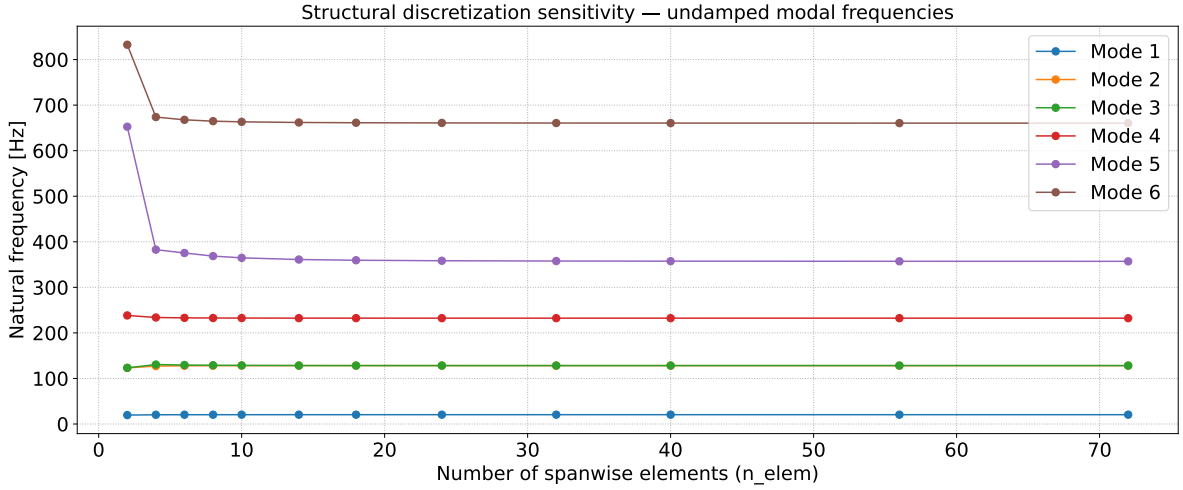

Figure 2.18: Structural discretization sensitivity for the undamped modal analysis. The first six natural frequencies are reported as functions of the number of spanwise elements n_{spanwise}. The trends show monotonic stabilization of the estimates, indicating that the lowest modes become mesh independent beyond moderate discretization levels.

The trends in Figure 2.18 show rapid convergence of the undamped natural frequencies with respect to the number of spanwise elements. The first three modes reach visually stable plateaus for $n_{\text{spanwise}} \geq 12$, while the fourth mode becomes effectively unchanged for $n_{\text{spanwise}} \geq 16$. Higher modes require a finer mesh, with modes five and six stabilizing only when $n_{\text{spanwise}} \geq 24$ to 32. Adopting a practical convergence criterion based on the relative change between successive refinements, the solution may be considered mesh independent for the first six modes when $n_{\text{spanwise}} = 32$. This value can be retained as a trade-off value of the study to balance accuracy and computational cost.

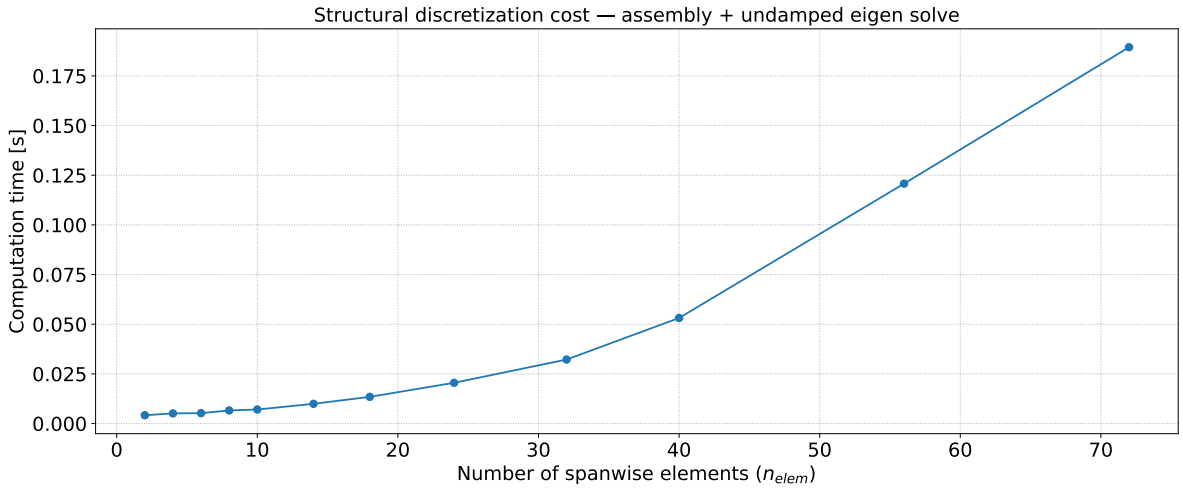

Figure 2.19: Computation time as a function of the number of spanwise elements n_{spanwise}. The measured cost includes the global matrix assembly and the undamped eigenvalue solution for the first six modes. The trends indicate that the computational framework sustains higher discretizations without a prohibitive increase in cost, which enables the use of refined meshes when required by accuracy considerations.

However, Figure 2.19 shows that the cost associated with the structural eigen-analysis grows moderately with the number of spanwise elements. Together with the frequency convergence in Figure 2.18, this confirms that discretizations beyond $n_{\text{spanwise}} = 32$ can be adopted without a prohibitive penalty. In the remainder of the study, a baseline mesh is selected for accuracy, while higher values are used when required for validation or for the analysis of higher modes.

The combination of Figures 2.18 and 2.19 demonstrates that the structural solver achieves rapid modal convergence while maintaining low computational cost, which allows the use of refined discretizations without compromising efficiency. Furthermore, the computational framework is specifically engineered for the highly efficient manipulation of large-scale matrices. The internal computational processes are performed primarily through array and matrix operations, minimizing the use of element-by-element loops. Consequently, this design ensures a high level of computational resource utilization, thereby enhancing effectiveness and time efficiency. These significant advantages will be substantiated throughout the thesis, particularly in the subsequent analyses of a real wing geometries, *ULiège*.

2.6.4 Modal Truncation Sensitivity in the Structural Solver

In the structural eigen-analysis, the system is projected onto a truncated modal basis of size n_{modes}. The value of n_{modes} directly influences the fidelity of the modal representation used for subsequent coupling and post-processing. If n_{modes} is too small, relevant dynamic features may be excluded, leading to biased frequency estimates and distorted mode shapes. Conversely, selecting unnecessarily large n_{modes} increases computational cost without meaningful gains for

the first modes of interest. In this subsection, the sensitivity of the natural frequencies to n_{modes} is assessed by monitoring the evolution of the first bending and torsional frequencies as n_{modes} is increased until convergence is observed within a prescribed tolerance.

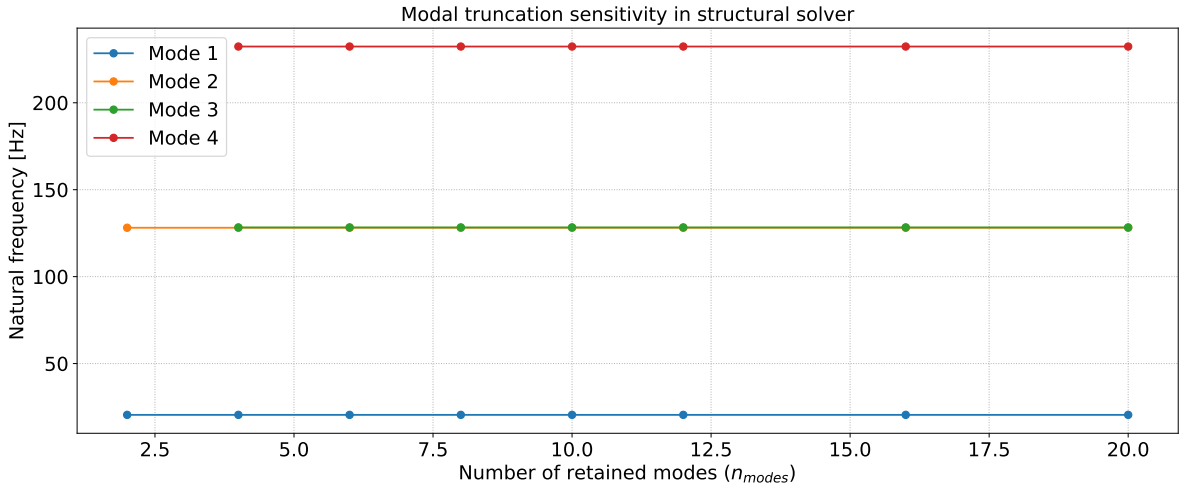

Figure 2.20: Sensitivity of the undamped natural frequencies to the number of retained modes n_{modes} in the structural solver. The first four frequencies remain constant once n_{modes} exceeds the index of the considered mode, showing that modal truncation does not affect the eigensolution for the lower bending and torsional modes.

The results of the truncation study are presented in Figure 2.20. It can be observed that the first four natural frequencies remain unchanged once the number of retained modes exceeds the corresponding modal index. In other words, convergence is achieved as soon as the modal basis is rich enough to include the targeted modes. No drift or spurious coupling is observed when increasing n_{modes} up to 20.

This confirms that the modal truncation has no impact on the fundamental bending and torsional modes that govern the aeroelastic response. Consequently, the selection of n_{modes} can be guided by practical considerations: it suffices to retain only the first few modes of physical interest, without risk of distortion in their frequency values. Larger truncations, while computationally affordable in the present solver, do not provide additional accuracy for these lower modes.

2.6.5 Aerodynamic Discretization Sensitivity

The reference NACA 0015 wing does not exhibit a flutter boundary in the studied range. To investigate the sensitivity of the aeroelastic solution to aerodynamic panelling, the well-documented AGARD 445.6 wing is adopted as a benchmark. This wing exhibits strong bending–torsion coupling and provides a well-established flutter boundary.

Figures 2.21 and 2.22 quantify the influence of aerodynamic panelling on the AGARD 445.6 flutter boundary. For chordwise refinement at fixed $n_{\text{half}} = 16$, the flutter speed grows from $U_F = 112.07$ m/s at $m = 8$ to $U_F = 113.47$ m/s at $m = 20$, after which the curve plateaus (no change at $m = 24$). For spanwise refinement at fixed $m = 20$, U_F increases from 112.16 m/s at $n_{\text{half}} = 8$ to 113.72 m/s at $n_{\text{half}} = 24$, with a clear flattening beyond $n_{\text{half}} \approx 20$. These trends indicate that mesh-independent estimates are obtained for $m \geq 20$ and $n_{\text{half}} \geq 20$; the total variation from very coarse to converged meshes is about 1–1.5%. Accordingly, the baseline aerodynamic discretization adopted in the remainder of this thesis is $m = 20$ and $n_{\text{half}} = 24$, which balances accuracy and cost while lying on the convergence plateau.

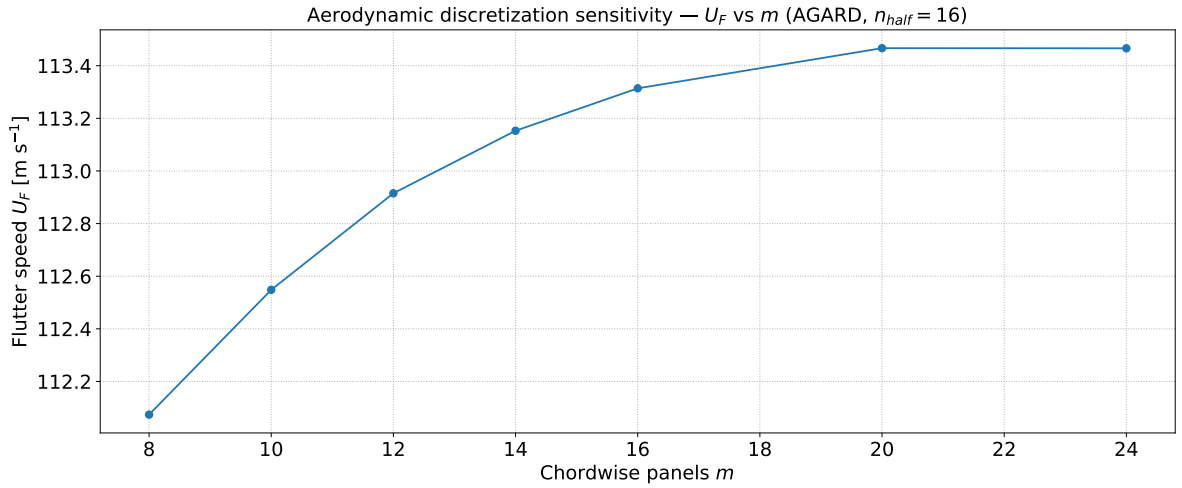

Figure 2.21: AGARD 445.6 flutter speed as a function of chordwise panels m, with spanwise resolution fixed at $n_{\text{half}} = 16$. Convergence is reached beyond $m \approx 20$.

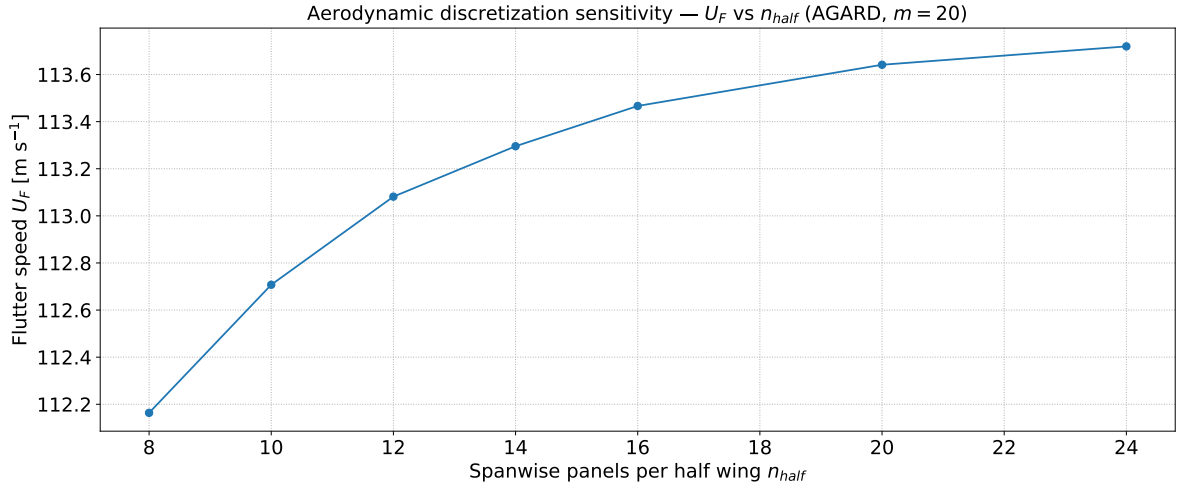

Figure 2.22: AGARD 445.6 flutter speed as a function of spanwise panels per half wing n_{half}, with chordwise resolution fixed at $m = 20$. The flutter speed becomes effectively mesh-independent beyond $n_{\text{half}} \approx 20$.

The sensitivity studies confirm that the computational framework produces mesh-independent predictions once moderate discretizations are adopted. The baseline values retained from this analysis are: $n_{\text{spanwise}} = 32$ for the structural beam, $n_{\text{modes}} = 6$ for the structural solver, and $(m, n_{\text{half}}) = (20, 24)$ for the aerodynamic discretization. These settings are used consistently in the following chapter to analyze the aeroelastic response of an experimental wing, namely the *ULiège* configurations.

Chapter 3

Results

3.1 ULiège Wing: Experimental and Numerical Comparison

In the scope of this section, the experimental and numerical investigations focus on the wing configuration developed and tested at the University of Liège (ULiège), which is documented in the master's thesis of Pirnay (2025) [7]. This configuration was specifically designed to expand the experimental dataset and to provide a basis for validating numerical models.

The design maintains the core characteristics of the IAT wing [7], including the NACA0015 airfoil sections and an aspect ratio of 15, but with a reduced half-span of 1.2 m to accommodate the smaller wind tunnel at Liège, for aeroelastic testing in the available facility. A solid aluminum rectangular beam was chosen as the internal structural component.

A summary of the key geometric and structural properties of the ULiège wing is presented in Table 3.1 below. These values serve as the foundation for the numerical model developed in the present thesis. The configuration is used here as the single reference case for all subsequent reconstructions, cross-sectional analyses, modal computations, and comparisons.

A schematic of the ULiège wing section assembly, highlighting the internal rectangular beam, is provided in Figure 3.1.

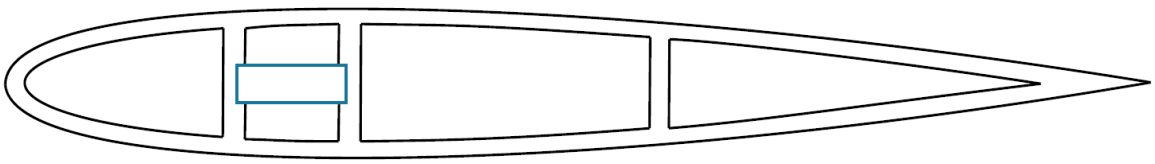

Figure 3.1: Schematic of the wing section assembly at ULiège. The blue region highlights the internal 6×15 mm rectangular beam, made of aluminium. (Source: [7], Figure 3.3).

Table 3.1: ULiège wing: consolidated geometric, structural, and cross-sectional data used in the numerical model. Source: [7].

Quantity	**Symbol**	**Value**	**Unit**
Geometry			
Airfoil	—	NACA 0015	—
Chord length	c	0.16	m
Full span	b	2.40	m
Semi-span (cantilever)	s	1.20	m
Aspect ratio	$AR = b/c$	15	—
Planform	—	Rectangular	—
Sweep / Dihedral	—	$0^\circ/0^\circ$	—
Number of spars	—	3	—
Spar chordwise locations	x_i/c	$\{0.20,\ 0.30,\ 0.57\}$	—
Main beam material	—	Aluminium	
Main beam dimensions	—	0.006×0.015	m
Skin / shell thickness	t_{skin}	0.003	m
Reference material (aluminium)			
Density	ρ	2700	$\mathrm{kg\,m^{-3}}$
Young's modulus	E	70	GPa
Poisson's ratio	ν	0.33	—
Sectional mass and inertia (per unit span)			
Mass per unit length	m	1.106	$\mathrm{kg\,m^{-1}}$
Polar moment about elastic axis (per unit length)	I_α	2.587×10^{-3}	$\mathrm{kg\,m^2 m^{-1}}$
Distance LE to elastic axis	X_{ea}	$c/4$	m
Distance LE to centre of gravity	X_{cg}	$0.41\,c$	m
Equivalent sectional stiffness			
Flapwise bending stiffness	EI_x	18.9	$\mathrm{N\,m^2}$
Chordwise bending stiffness	EI_z	118.12	$\mathrm{N\,m^2}$
Torsional stiffness	GJ	21.27	$\mathrm{N\,m^2}$

Values for m, I_α, EI_x, EI_z, and GJ correspond to the experimental configuration reported by Pirnay [7]. The spar positions $\{0.20, 0.30, 0.57\}\,c$ are set during the cross-section reconstruction in the computational framework and may be refined in the sensitivity study.

3.1.1 Cross-Sectional Model Reconstruction

The geometric and structural properties outlined in Table 3.1 serve as the foundational input for the cross-sectional model developed within the present computational framework. The reconstruction process is performed in a progressive and physically meaningful sequence, starting with the fundamental airfoil profile and incrementally adding the internal structural components. This approach ensures that the resulting model accurately represents the geometry of the physical wing tested at ULiège.

Initial Airfoil Reconstruction and Hollowing

The reconstruction begins by loading the coordinate data for the NACA 0015 airfoil from a standard `.dat` file. This raw geometry is scaled to the specified chord length of $c = 0.16\,\mathrm{m}$ to establish the outer contour, as shown in Figure 3.2a. Subsequently, the exterior profile is offset by a specified skin thickness of $3\,\mathrm{mm}$ to create a hollow, thin-walled contour shell. This operation accurately captures the primary load-bearing surface of the wing and provides the base geometry for all subsequent internal additions, as illustrated in Figure 3.2b. This step is a direct implementation of the defined inputs and sets the stage for the detailed internal structure.

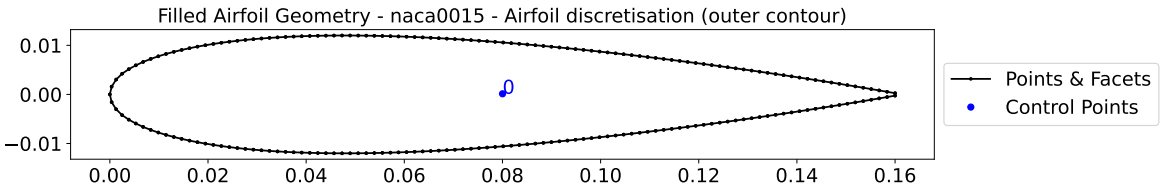

(a) Initial NACA 0015 airfoil outer contour.

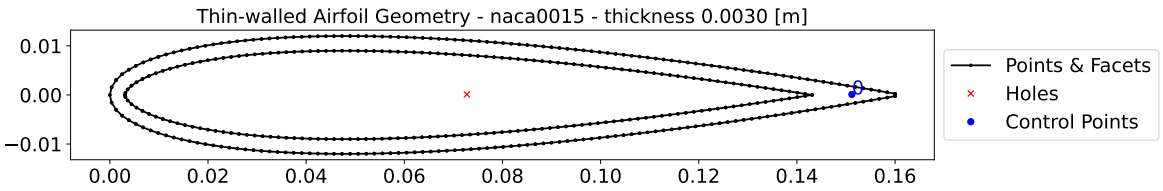

(b) Hollow NACA 0015 airfoil section with 3mm skin.

Figure 3.2: Reconstruction of the ULiège wing cross-section: Initial steps, Reconstruction and Hollowing.

Incorporation of Spars and Main Beam

The next phase involves integrating the internal stiffening components, specifically the three spars and the main aluminum beam. Three spars are defined as rectangular sections at the chordwise locations provided in Table 3.1. Their geometry is automatically generated, within the computational framework, and positioned within the hollow airfoil profile, as shown in Figure 3.3a. The central aluminum beam, which serves as the primary structural element, on which the elastic axis lies, is then added in the chordwise region between the first and second spars. This beam is assigned the material properties of aluminum, as specified in the reference thesis [7]. The combination of these components results in a complete, composite cross-section that can be further analyzed. The final reconstructed cross-section with all components is depicted in Figure 3.3b.

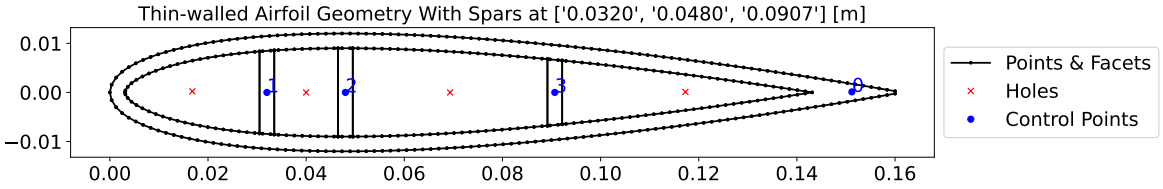

(a) Thin-walled airfoil with three internal spars.

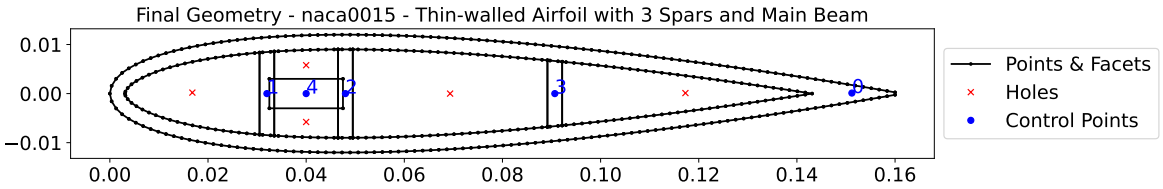

(b) Final geometry with the main aluminum beam.

Figure 3.3: Reconstruction of the ULiège wing cross-section: Addition of internal structures.

Advanced Cross-Sectional Analysis

Following the geometric reconstruction, a detailed cross-sectional analysis is performed to determine the key geometric and warping properties. The computational framework employs an advanced meshing algorithm to discretize the complex geometry, as have been stated previously, and as shown in Figure 3.4a, ensuring high accuracy in the calculation of properties such as the centroid and shear center. The material properties (Young's modulus, Poisson's ratio, and density) are assigned to each geometric region, and a finite element-based solver is utilized to

compute the mass, stiffness, and warping characteristics.

A notable distinction arises when **comparing the results** of this **advanced** analysis with the **simplified** assumptions made in the reference thesis [7]. For instance, the reference thesis states the mass center of gravity (CG) to be at $X_{cg} = 0.41\,c$, a value likely derived from simplified theoretical models, refer to [8] . In contrast, in the present computational framework yields a more precise value of $X_{cg} = 0.44\,c$. This discrepancy is not an error but a direct consequence of using a more sophisticated and physically realistic modeling approach.

As discussed in Appendix C of the reference thesis [7], simplified theoretical expressions were used for stiffness assessment, while the present methodology employs a detailed meshing of the entire cross-section to perform an integrated finite element analysis. This advanced approach provides a more accurate representation of the inertial and elastic properties. Figure 3.4b presents the final meshed cross-section with the computed reference points (centroid and shear center).

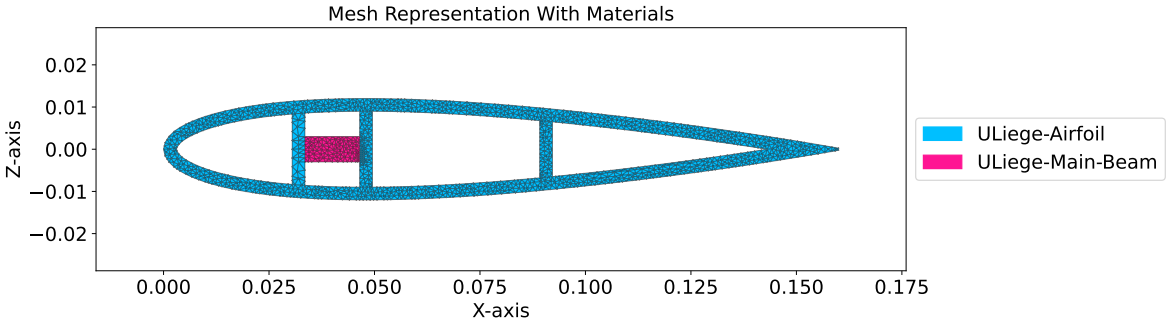

(a) Final meshed cross-section with material assignments.

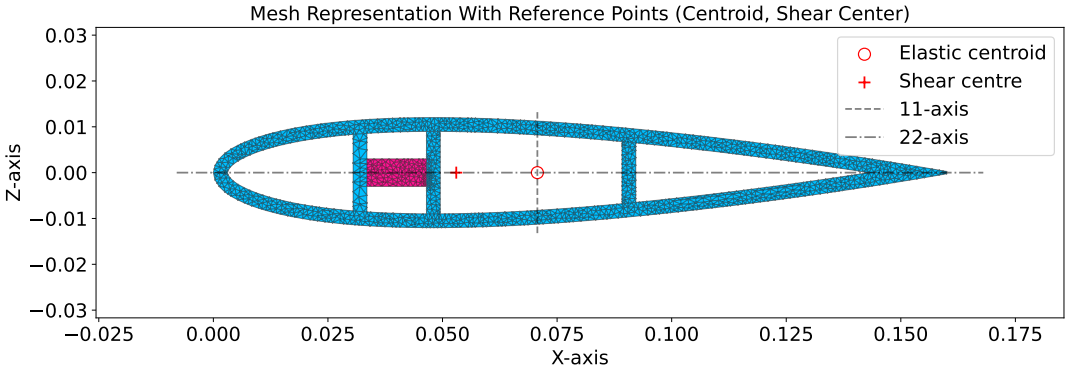

(b) Final meshed cross-section showing the computed centroid and shear center.

Figure 3.4: Cross-sectional analysis results.

3.1.2 Cross-Sectional Analysis: Numerical Outputs and Comparison

This subsection reports the near-exact cross-sectional outputs delivered by the computational framework for the ULiège wing. The geometry corresponds to the hollow NACA 0015 airfoil, as previously discussed, with trailing-edge closure, three spars at $x/c = \{0.20, 0.30, 0.57\}$, and an aluminium main beam between spars 1 and 2, discretised with a mesh size selected from a convergence study. The quantities in Table 3.2 include mass and geometric metrics, centroid and shear centre, second moments and torsion constant, and the equivalent stiffnesses EI_x, EI_z, and GJ. For context, the reduced parameters reported by Pirnay [7] are shown alongside the present values. The two sets reflect **different** modelling assumptions, **therefore the comparison is descriptive rather than an error metric**, and the present figures are taken as high-fidelity inputs for the subsequent modal and aeroelastic analyses.

Table 3.2: ULiège wing cross-sectional properties: near-exact values from the computational framework and the reduced parameters reported by Pirnay [7]. The two sets serve different modelling purposes and are not intended as an error metric.

Quantity	**Symbol**	**Present (near-exact)**	**Unit**	**Pirnay [7]**
Geometry and mass (per unit span)				
Elastic axis (from LE)	X_{ea}/c	0.25	—	0.25
Centre of gravity (from LE)	X_{cg}/c	0.4419	—	0.41
Shear centre (from LE)	X_{sc}/c	0.3290	—	—
Mass per unit length	m	1.105	$\mathrm{kg\,m^{-1}}$	1.106
Net section area	A	1.149×10^{-3}	$\mathrm{m^2}$	—
Skin perimeter	P	0.3295	m	—
Sectional inertia and torsion				
Second moment (flapwise axis)	I_x	5.896×10^{-8}	$\mathrm{m^4}$	—
Second moment (chordwise axis)	I_z	2.048×10^{-6}	$\mathrm{m^4}$	—
Torsion constant	J	2.049×10^{-7}	$\mathrm{m^4}$	—
Equivalent sectional stiffness				
Flapwise bending stiffness	EI_x	18.986	$\mathrm{N\,m^2}$	18.9
Chordwise bending stiffness	EI_z	659.573	$\mathrm{N\,m^2}$	118.12
Torsional stiffness	GJ	24.435	$\mathrm{N\,m^2}$	21.27
Shear characteristics (solver outputs)				
Shear area (flapwise)	$A_{s,x}$	7.812×10^{-4}	$\mathrm{m^2}$	—
Shear area (chordwise)	$A_{s,z}$	1.550×10^{-4}	$\mathrm{m^2}$	—

Notes: present values are mesh-resolved and geometry-conforming (hollow skin with trailing-edge closure, three spars, explicit aluminium main beam). Pirnay's figures [7], are the reduced parameters used in the experimental modelling and are shown for context only.

As it can be seen from Table 3.2), a side-by-side with the reduced parameters reported by Pirnay [7] is informative yet not an error metric. The reference parametrisation employs simplified geometric and torsional representations intended for reduced-order modelling and test planning.

The present computational framework resolves the full two-dimensional section, including finite skin thickness, trailing-edge closure, and internal members, which shifts the centre of gravity from $0.41\,c$ to $0.4419\,c$ and increases the chordwise stiffness. The marked difference in EI_z reflects these modelling choices and the explicit distribution of material about the chordwise axis. The comparison documents assumptions while the present figures are taken as near-exact within the numerical tolerance.

The locations of the centroid and shear centre are critical for the aeroelastic coupling. With $X_{cg}/c = 0.4419$ and $X_{sc}/c = 0.3290$, the centre of gravity lies **aft** of the shear centre.
Under positive lift, this arrangement introduces a nose-down torsional moment that magnifies **bending – torsion coupling** as the dynamic pressure increases. The offset also influences the relative contribution of chordwise bending and torsion in the low-frequency modes, which will be visible in the mode-shape visualisations later on, in the modal analysis.

Bending-Torsion Flutter

Bending-torsion flutter, the most standard form of dynamic aeroelastic instability in aircraft wings, arises from a resonant coupling between the wing's bending and torsional modes. This instability is particularly sensitive to the proximity of these modes' natural frequencies, as close frequencies facilitate a more efficient energy exchange between the structural deformations. Classical bending–torsion flutter mechanisms and reduced-frequency effects are comprehensively documented in standard references [1], [2], [5].

The fundamental mechanism for this interaction is based on the relative chordwise locations of three critical axes: the **elastic** axis, the **inertial** axis, and the **aerodynamic** axis. The elastic axis is the line along the span about which the wing twists without bending. The inertial axis passes through the center of gravity (CG) of each wing section, representing the location of the inertial forces. Finally, the aerodynamic axis (or aerodynamic center) is the point where the aerodynamic lift is considered to act, typically near the quarter-chord.

The intentional misalignment of the elastic axis and the inertial axis is a key design feature that promotes this coupled dynamic behaviour. As the wing bends, the inertial forces act about the offset inertial axis, inducing a pitching moment that excites the torsional mode. This, in turn, alters the wing's angle of attack and changes the aerodynamic forces, creating a **positive feedback loop** that can lead to divergent oscillations. Various configurations of these axes can be defined, each leading to a different stability profile, as conceptually illustrated here below in Figure 3.5.

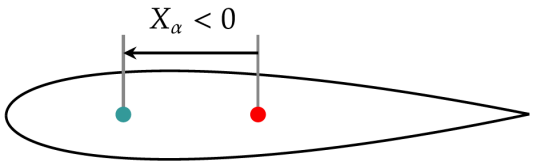

(a) Case (a): Inertial axis forward of the elastic axis, a **unconditionally stable** configuration.

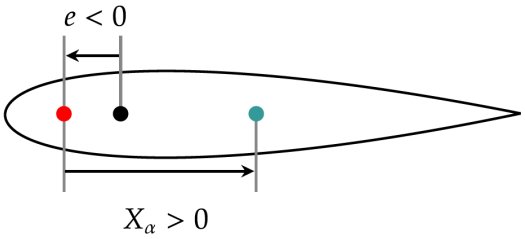

(b) Case (b): Inertial axis aft of the elastic axis, an **unconditionally unstable** configuration.

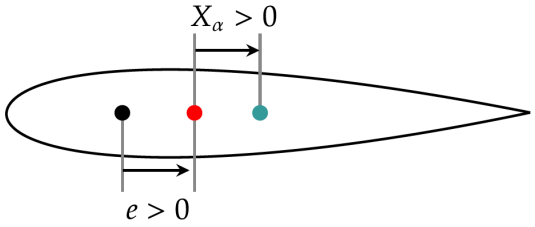

(c) Case (c): All three axes aligned, a **conditionally stable** configuration.

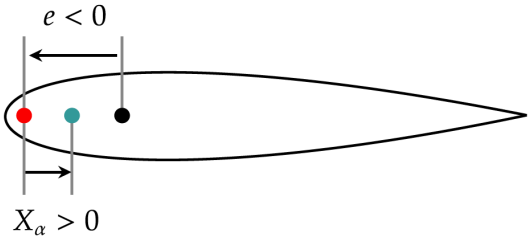

(d) Case (d): A complex alignment leading to specific flutter conditions.

Figure 3.5: Configurations leading to coupled-mode flutter, illustrating the relative positions of the elastic axis (•), inertial axis (•), and aerodynamic axis(•).

In-plane & Out-of-plane Modes

The structural eigenproblem analysis retrieves both out-of-plane and in-plane families. The **planar** modes are captured, by the computational framework, because the three-dimensional beam model resolves all translational components and reconstructs rotations from displacement gradients. For aeroelastic studies, modes with negligible out-of-plane displacement and torsion do not contribute meaningfully to the lifting-surface unsteady aerodynamics. A filtering step is therefore applied that excludes modes with vanishing vertical displacement or negligible torsional content. Negligible means, in this context, that any displacement below a certain zero-tolerance limit, such as 10^{-8} for most engineering applications, specially here in aeroelasticity, is considered as zero displacement [1].

An illustration of a planar mode, captured at low frequency, can be seen in Figure 3.7.

Therefore, based on the fact that all the natural frequencies have been correctly captured by the modal eigenproblem solver, as it will be seen in section 3.1.5, the results confirms that the computed chordwise bending stiffness, EI_z, is correct and accurate.

The following section initiates the **modal** analysis by defining the structural grid and presenting the initial undeformed shape, which forms the basis for the undamped and Rayleigh-damped eigenvalue solvers.

3.1.3 Modal Analysis: Structural Model and Eigenvalue Problem

The structural discretisation employed for the half-wing is a spanwise–chordwise lattice of $n_{\text{span}} \times n_{\text{chord}} = 100 \times 20$ nodes. The node positions follow the geometric planform and the internal layout established in the cross-sectional reconstruction, ensuring consistency of mass and stiffness distributions along the span. This grid provides the kinematic basis for the eigenvalue problems solved in the next steps, first in the undamped case and subsequently with proportional (Rayleigh) damping.

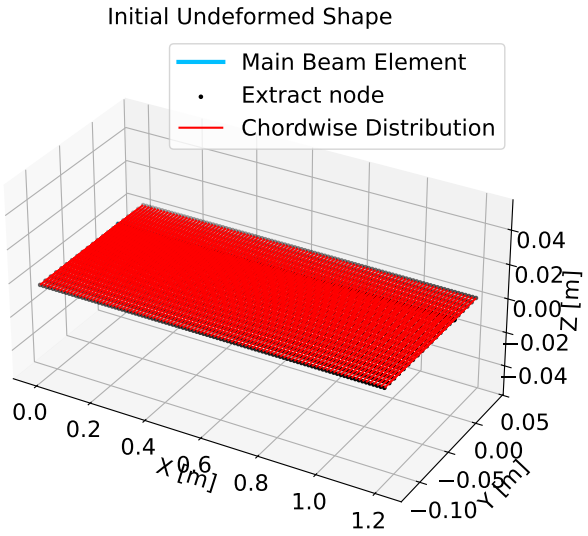

Figure 3.6: Initial undeformed shape and structural lattice with $n_{\text{span}} \times n_{\text{chord}} = 100 \times 20$ nodes.

3.1.4 Modal formulation: undamped and Rayleigh-damped problems

The structural dynamics of the discretised wing are obtained from the second-order system

$$\mathbf{M}\,\ddot{\mathbf{q}} + \mathbf{C}\,\dot{\mathbf{q}} + \mathbf{K}\,\mathbf{q} = \mathbf{0}\,, \tag{3.1}$$

with mass matrix $\mathbf{M}$, proportional damping $\mathbf{C} = \alpha\,\mathbf{M} + \beta\,\mathbf{K}$, and stiffness matrix $\mathbf{K}$.

Undamped eigenproblem: Setting $\mathbf{C} = \mathbf{0}$ yields the generalised eigenproblem :

$$\mathbf{K}\,\boldsymbol{\phi}_r = \omega_r^2\,\mathbf{M}\,\boldsymbol{\phi}_r, \qquad \boldsymbol{\phi}_r^{\top}\mathbf{M}\,\boldsymbol{\phi}_r = 1, \tag{3.2}$$

providing natural frequencies ω_r and mass-normalised mode shapes $\boldsymbol{\phi}_r$.

Rayleigh-damped eigenproblem: With $\mathbf{C} = \alpha\,\mathbf{M} + \beta\,\mathbf{K}$, the quadratic eigenvalue problem :

$$(\mathbf{K} + \mathrm{i}\omega\,\mathbf{C} - \omega^2\mathbf{M})\,\hat{\boldsymbol{\phi}} = \mathbf{0}\,, \tag{3.3}$$

is solved (equivalently via first-order state-space form). Given two target modal damping ratios ζ_1, ζ_2 at ω_1, ω_2, the Rayleigh coefficients follow from :

$$\zeta(\omega) = \tfrac{1}{2}\Big(\tfrac{\alpha}{\omega} + \beta\,\omega\Big), \quad \Rightarrow \quad \beta = \frac{2(\zeta_2\omega_2 - \zeta_1\omega_1)}{\omega_2^2 - \omega_1^2}, \qquad \alpha = \frac{2\,\omega_1\omega_2\,(\zeta_1\omega_2 - \zeta_2\omega_1)}{\omega_2^2 - \omega_1^2}. \tag{3.4}$$

In practice, (ω_1, ω_2) are selected as the first bending and first torsion frequencies, and (ζ_1, ζ_2) are set either from measurements or from nominal structural damping levels (0.3–1%) when measurements are unavailable.

3.1.5 Natural frequencies: numerical vs experimental (first four non-planar modes)

Modes with negligible out-of-plane displacement or torsion were classified as planar and excluded from the aeroelastic set. In the present computation, the second mode ($\approx 9.01\,\mathrm{Hz}$) is planar and was filtered out before comparison. Table 3.3 compares the first four non-planar natural frequencies with Pirnay's experimental values [7].

Table 3.3: First four **non-planar** natural frequencies of the ULiège wing: numerical vs experimental values from Pirnay [7]. Relative difference is $(f_{\text{num}} - f_{\text{exp}})/f_{\text{exp}} \times 100\%$. Grid 100×20.

Mode	Description	f_{exp} [Hz]	f_{num} [Hz]	$\Delta\%$
1	Bending-dominant (flapwise)	1.803	1.6099	-10.709
2	Bending/Torsion mixed (Second Bending)	10.069	10.0651	-0.0386
3	Bending/Torsion mixed (First Torsion)	22.879	22.8760	-0.0133
4	Bending-dominant, higher frequency	27.895	28.0811	$+0.6671$

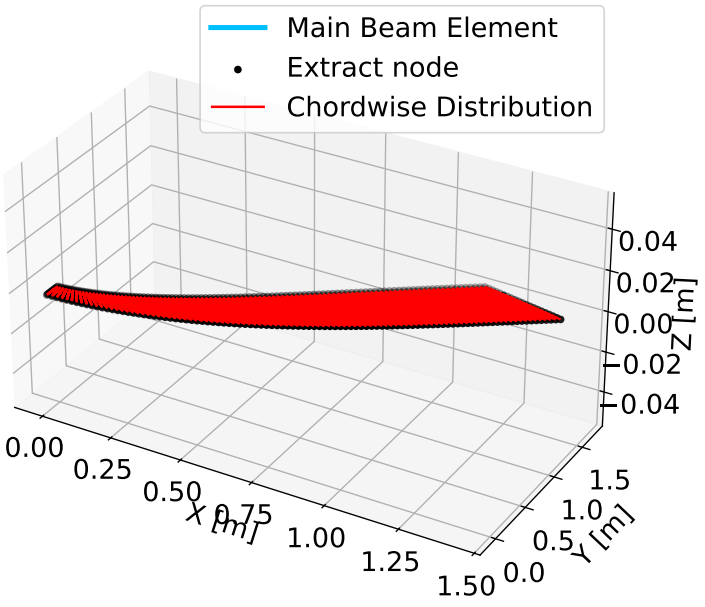

Figure 3.7: Planar mode at $9.01\,\mathrm{Hz}$ (filtered out). Grid 100×20.

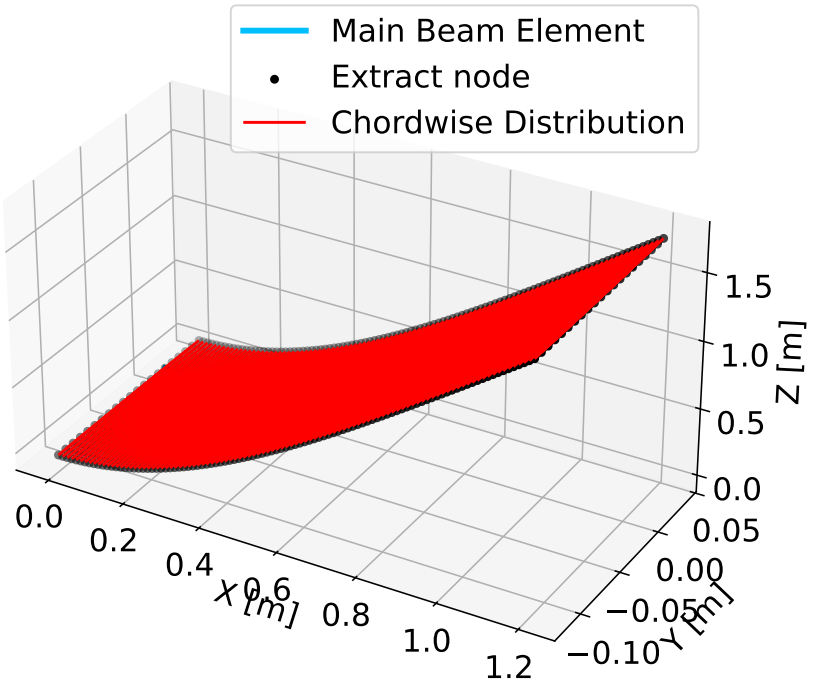

Figure 3.8: Mode 1 (non-planar), $f_{\text{num}} \approx 1.61\,\text{Hz}$. Grid 100×20.

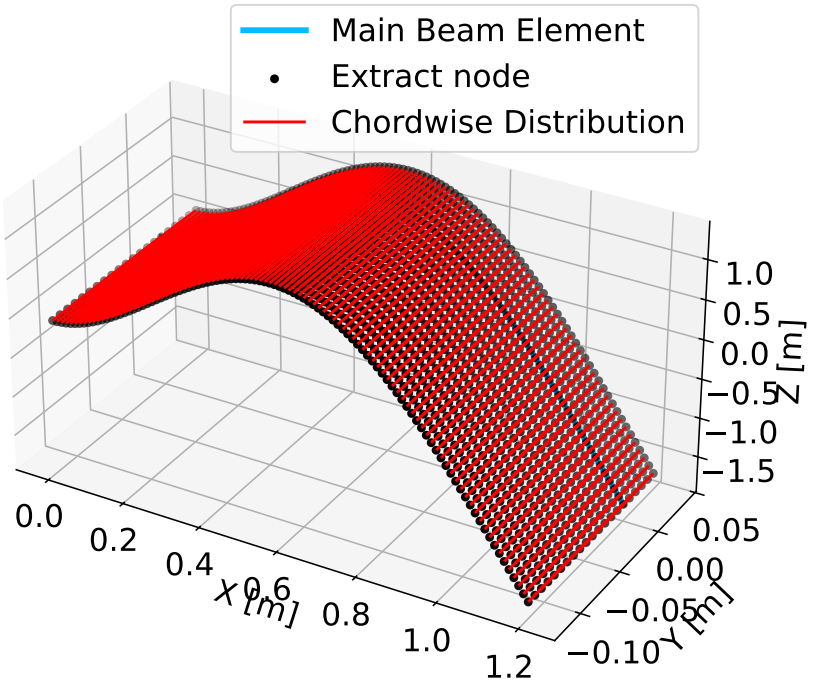

Figure 3.9: Mode 2 in the non-planar set, $f_{\text{num}} \approx 10.06\,\text{Hz}$. Grid 100×20.

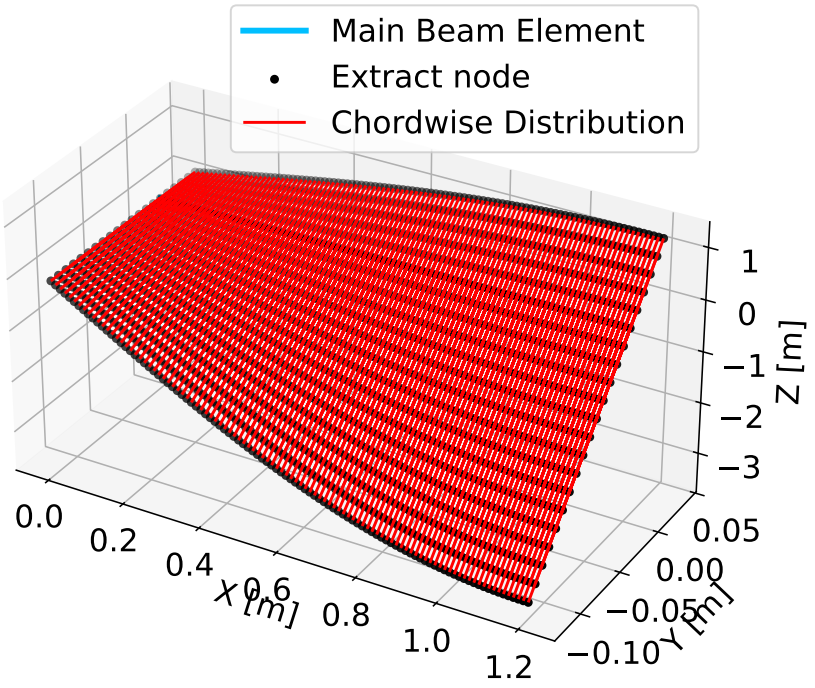

Figure 3.10: Mode 3 in the non-planar set, $f_{\text{num}} \approx 22.88\,\text{Hz}$. Grid 100×20.

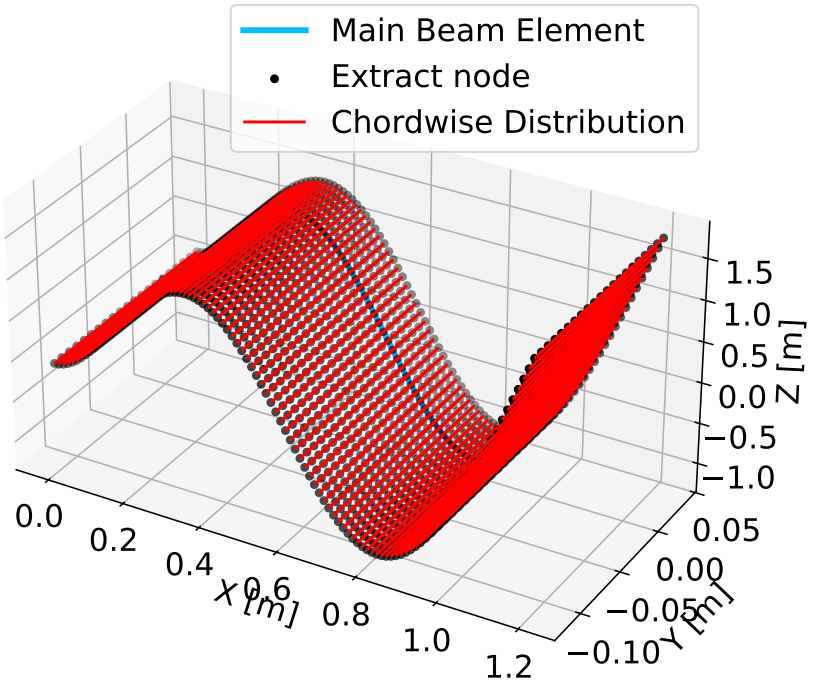

Figure 3.11: Mode 4 in the non-planar set, $f_{\text{num}} \approx 28.07\,\text{Hz}$. Grid 100×20.

3.1.6 Damping model: Rayleigh coefficients and damped modal set

Proportional damping is introduced as $\mathbf{C} = \alpha\,\mathbf{M} + \beta\,\mathbf{K}$. Two target modal damping ratios are prescribed to determine α and β via (3.4). The first bending frequency is taken as $f_1 = 1.6099\,\mathrm{Hz}$ and the first torsion (mixed) as $f_\alpha = 22.8760\,\mathrm{Hz}$. With nominal targets $\zeta_1 = 0.5\%$ at f_1 and $\zeta_\alpha = 0.3\%$ at f_α, the Rayleigh coefficients evaluate to :

$$\alpha = 9.736 \times 10^{-2}\ \mathrm{s}^{-1}\ , \qquad \beta = 3.703 \times 10^{-5}\ \mathrm{s}\ .$$

These values imply the frequency-dependent law $\zeta(\omega) = \frac{1}{2}(\alpha/\omega + \beta\,\omega)$. The resulting predicted damping ratios for the first four non-planar modes are listed in Table 3.4. If measured structural damping is available, (ζ_1, ζ_α) can be replaced directly and the coefficients updated.

Table 3.4: Predicted modal damping ratios with Rayleigh damping $\alpha = 9.736 \times 10^{-2}\ \mathrm{s}^{-1}$, $\beta = 3.703 \times 10^{-5}\ \mathrm{s}$. Targets were $\zeta_1 = 0.5\%$ at $f_1 = 1.6099\,\mathrm{Hz}$ and $\zeta_\alpha = 0.3\%$ at $f_\alpha = 22.8760\,\mathrm{Hz}$.

Mode (non-planar set)	$\mathbf{f_{num}}$ **[Hz]**	$\boldsymbol{\zeta}$ **[–]**	$\boldsymbol{\zeta}$ **[%]**
1 (Bending-dominant)	1.6099	0.00500	0.50
2 (Second Bending / mixed)	10.0651	0.00194	0.194
3 (First Torsion / mixed)	22.8760	0.00300	0.30
4 (mixed, higher frequency)	28.0811	0.00354	0.354

The Rayleigh pair (α, β) anchors the damping at the second bending and first torsion while producing smooth interpolation across the remaining spectrum. The damped modal set will be used in the aeroelastic comparison below.

3.1.7 Aeroelastic Comparison: Frequencies and Damping vs Airspeed

The structural modal basis defined in Sections 3.1.5–3.1.6 is coupled to the unsteady aerodynamic model using the `SDPMflut` software. Predictions are reported as functions of the tunnel airspeed U, and compared with the experimental points documented by Pirnay [7]. The plots show the evolution of the first second bending and the first torsion (mixed) branches. Planar modes are excluded from the comparison as discussed previously. This constitutes an important critical step, in the scope of this thesis, since it represents the **validation of the computational framework**.

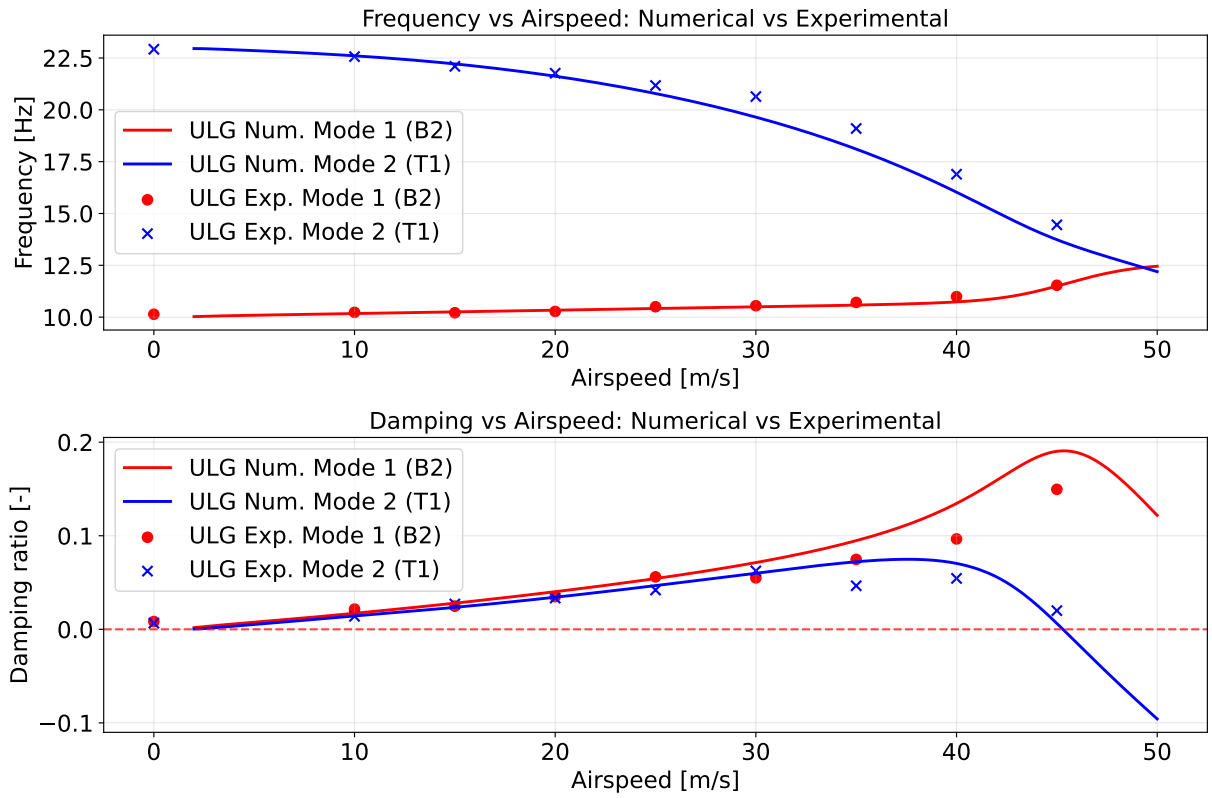

Figure 3.12: Comparison of numerical predictions with experimental results for the ULiège wing: evolution of natural frequencies (top) and damping ratios (bottom) with airspeed. Numerical predictions are shown as continuous curves, experimental points from Pirnay [7] as markers. Planar modes were excluded as discussed in Section 3.1.5. The red curve (———) represents the second bending mode (B2), the blue curve (———) represents the first torsion (T1).

The upper plot in Figure 3.12 shows the evolution of the second bending (B2) and first torsion (T1) natural frequencies with airspeed. The numerical model correctly captures the experimentally observed trends for both modes. The bending mode's frequency remains relatively constant, while the torsional mode's frequency, initially higher, decreases as airspeed increases. This phenomenon, known as aerodynamic softening, is a direct consequence of the unsteady aerodynamic forces acting on the structure. The model successfully predicts this progressive convergence of the two modes, which is a precursor to flutter instability. The close alignment between the numerical curves and the experimental points, up to approximately $U = 35\,\mathrm{m/s}$ demonstrates the model's robustness and its capacity to predict the coupled frequency behaviour with high fidelity.

The lower plot in Figure 3.12 shows the corresponding evolution of the damping ratios. The numerical model captures the overall trends of the experimental data with good agreement, especially for the torsional mode (T1). A key observation is the initial increase in damping for both modes at low airspeeds, followed by a decline as the modes begin to interact. The damping

ratio of the torsional mode decreases as it approaches the bending mode's frequency. The model predicts a sharp decrease in the damping of this mode as the airspeed approaches the flutter speed, with the damping becoming negative beyond $U \approx 45.8\,\mathrm{m/s}$. This behaviour, where one mode's damping decreases while another's increases, is characteristic of flutter instability and aligns with the theoretical principles of aeroelastic coupling. While there is a slight gap between the numerical curves and the experimental points, this discrepancy is acceptable and is expected due to a number of factors, including:

- **Structural and Material Uncertainties**:
  Minor variations in material properties, manufacturing tolerances, and the clamping conditions of the physical wing can lead to deviations from the idealized numerical model.
- **Experimental Measurement Limitations**:
  The accuracy of sensor data, signal processing techniques, and ambient noise during wind tunnel tests can introduce small uncertainties into the experimental results.
- **Aerodynamic Assumptions**:
  The numerical model, based on the unsteady Theodorsen theory, within `SDPMflut`, makes certain assumptions, naming (inviscid, irrotational and isentropic flow assumptions. Small perturbations, potential flow where the flow remains attached to the surface and separated smoothly at the trailing edge) that may not perfectly capture the complex real-world flow physics.

The numerical model's predicted flutter speed of $U_{crit} \approx 45.8\,\mathrm{m/s}$ is in excellent agreement with the experimentally observed flutter onset, which occurred in the range of 45 to $47.5\,\mathrm{m/s}$. The model slightly under-predicts this value, but the overall behaviour is well-captured. The consistency between the numerical and experimental results confirms the **validity** of the modeling methodology and its suitability for predicting the aeroelastic behaviour of the ULiège wing. In the following sections, a detailed sensitivity analysis will be performed to quantify the impact of these identified uncertainties on the aeroelastic predictions.

3.2 Uncertainty Analysis

This section quantifies how plausible variations in aerodynamic and structural inputs affect the predicted frequencies and damping versus airspeed. **Envelopes** will be constructed by varying one parameter at a time around the nominal model and plotting the resulting upper/lower contours of the frequency- and damping- airspeed curves. The nominal model is the high-fidelity reconstruction reported in Section 3.1.2 and used in the modal/aeroelastic validation.

3.2.1 Methodology and parameter bounds

The envelope curves are generated as follows: (i) select a parameter and a symmetric bound around the nominal, (ii) re-solve the cross-section (when structural) and the aeroelastic problem, (iii) retain, at each airspeed U, the pointwise minimum and maximum across the varied cases.

Three categories are considered:

- **Aerodynamic:** free-stream density ρ, Mach M, and panelling (chordwise/spanwise) that affects the unsteady load resolution.
- **Structural:** mass per unit span m, bending/torsional stiffnesses EI_x, GJ, and the chordwise placement of the centre of gravity X_{cg}/c .
- **Damping:** Rayleigh targets (ζ_1, ζ_α) for first bending and first torsion, propagated via $\mathbf{C} = \alpha\mathbf{M} + \beta\mathbf{K}$.

Table 3.5 summarises the nominal values and the bounds used to build the envelopes. The levels reflect typical fabrication scatter and identification variability, they can be tightened/relaxed if laboratory characterisations are available.

Table 3.5: Nominal values and uncertainty bounds used for envelope construction.

Parameter	Symbol	Nominal	Bound	Rationale
Air density	ρ	$1.225\ \mathrm{kg\,m^{-3}}$	$\pm 5\%$	Tunnel conditions
Mach number	M	0.10	± 0.02	Speed set-point
Chordwise panels (aero)	m	10	$\{8, 12\}$	Load resolution
Spanwise panels/half (aero)	n_{half}	10	$\{8, 12\}$	Wake/induction resolution
Mass per unit span	m	$1.105\ \mathrm{kg\,m^{-1}}$	$\pm 5\%$	Inserts/bonding scatter
Flapwise stiffness	EI_x	$18.986\ \mathrm{N\,m^2}$	$\pm 10\%$	Shell thickness, spars
Torsional stiffness	GJ	$24.435\ \mathrm{N\,m^2}$	$\pm 10\%$	Skin closure/beam fit
CG location (from LE)	X_{cg}/c	0.4419	± 0.01	Root hardware placement
Rayleigh target (bend)	ζ_1	0.5%	$\pm 0.2\%$	Structural damping ID
Rayleigh target (torsion)	ζ_α	0.3%	$\pm 0.2\%$	Structural damping ID

Aerodynamic sensitivity: Mach and discretisation

Figure 3.13 shows the impact of varying the free-stream Mach number by ± 0.02 about the nominal $M = 0.10$. The frequency curves are only weakly affected, while the damping curves shift visibly in the mid–high speed range, consistent with changes in the unsteady load phase (Prandtl–Glauert scaling and reduced frequency effects). The onset of instability is essentially governed by the damping trend. The envelope width remains moderate and compatible with tunnel set-point uncertainty.

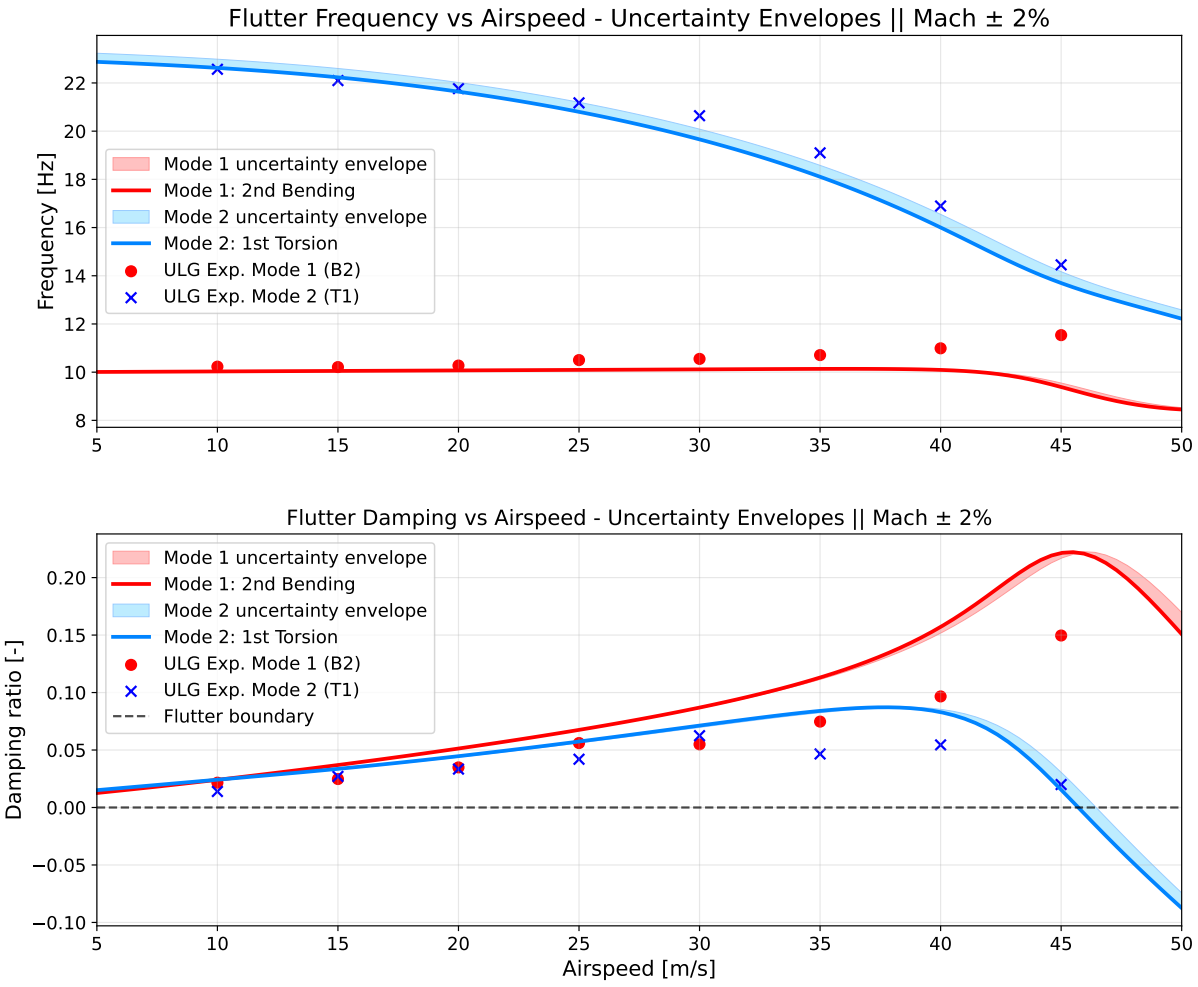

Figure 3.13: Effect of Mach uncertainty ($M = 0.10 \pm 0.02$): frequency (top) and damping (bottom) versus airspeed. The nominal curve lies between the upper/lower contours, markers ($\times$, $\bullet$) indicate experimental points [7].

Figure 3.14 illustrates the discretisation sensitivity by coarsening/refining the aerodynamic lattice (chordwise/half-span counts). The frequency and damping curves are stable under these changes, the band is thin across all U, indicating that the nominal discretisation already lies in the converged regime. This justifies using the nominal panelling for all subsequent comparisons.

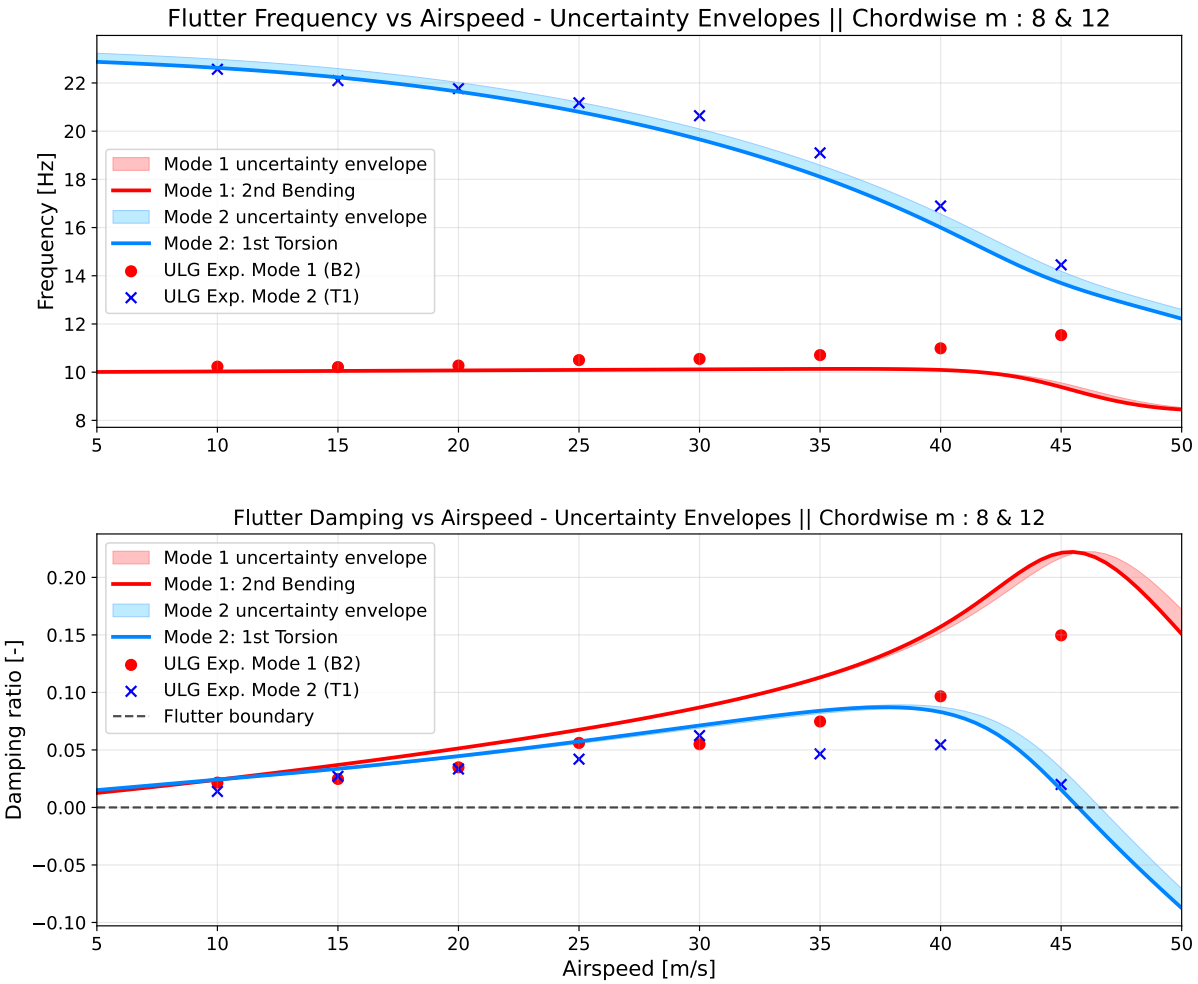

Figure 3.14: Aerodynamic discretisation effect (panel counts varied around the nominal). The envelope remains narrow, showing minimal sensitivity to the chosen grid resolution.

Aerodynamic inputs primarily influence the **damping** parameter, frequencies are comparatively rigid. The discretisation study confirms the numerical robustness of the nominal aero mesh.

Structural sensitivity: mass and stiffness placement

Figure 3.15 reports the effect of $\pm 5\%$ variation in the mass per unit span. As expected from $\omega \sim \sqrt{K/M}$, the first bending-dominant frequency shifts most, and the associated damping curve moves accordingly near the onset region. The torsion branch is less sensitive to m, except through coupling.

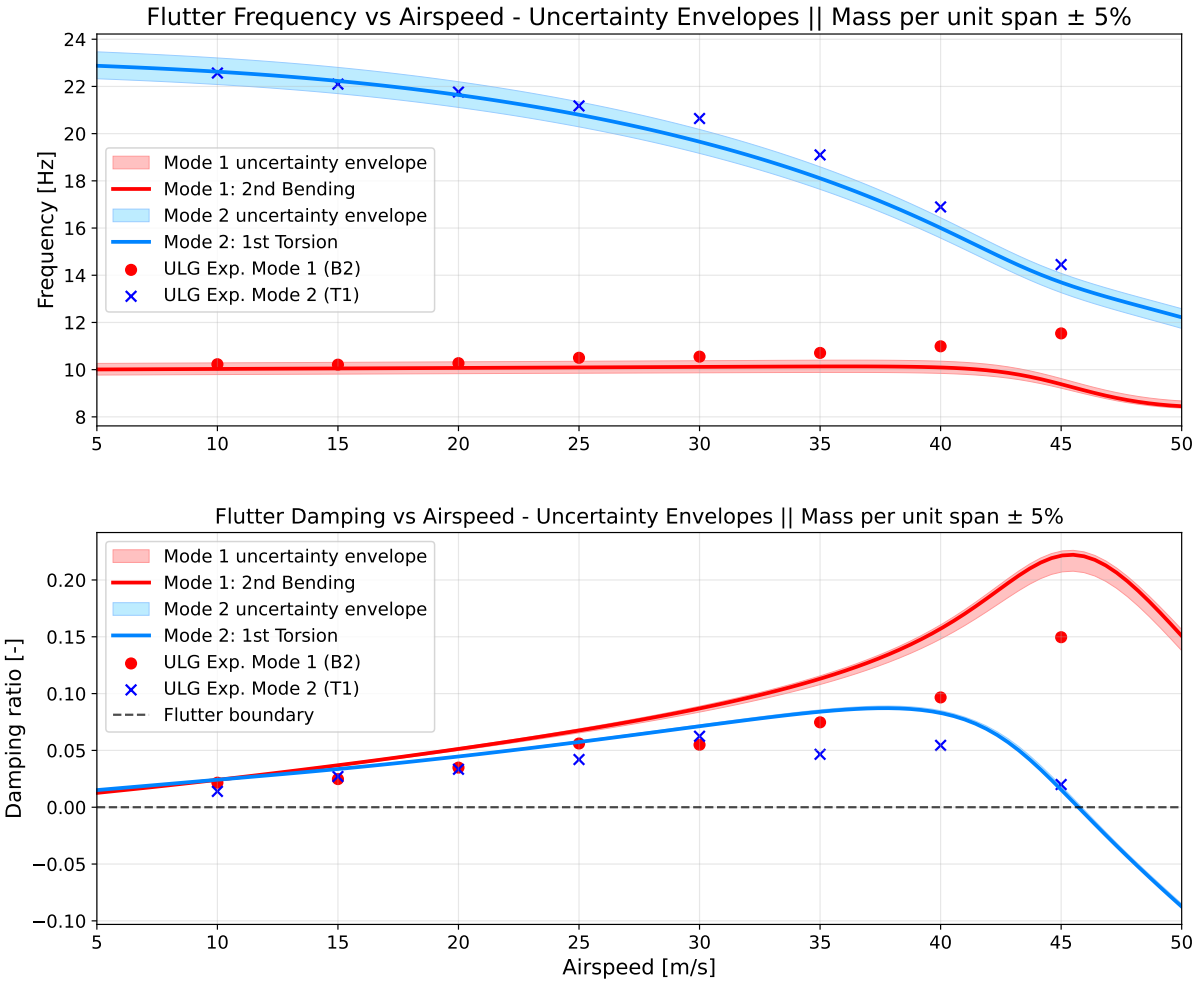

Figure 3.15: Effect of mass uncertainty ($m = \text{nominal} \pm 5\%$). Bending frequency and its damping are most affected, torsion is comparatively insensitive apart from coupling.

Figures 3.16 and 3.17 isolate bending and torsional stiffness. Increasing EI_x ($\pm 10\%$) raises bending-dominant frequencies and tightens the damping trend in the pre-flutter regime. Increasing GJ ($\pm 10\%$) lifts the torsion branch and reduces bending-torsion proximity, which generally delays destabilisation (narrower negative-damping excursion or a right-shift of the onset). These trends are coherent with the frequency placement ratio f_h/f_α discussed in Section 3.2.2.

Structural parameters control the **frequency placement** and coupling. EI_x tunes the bending line, GJ governs the torsion branch and the separation f_h/f_α, which is directly tied to flutter susceptibility.

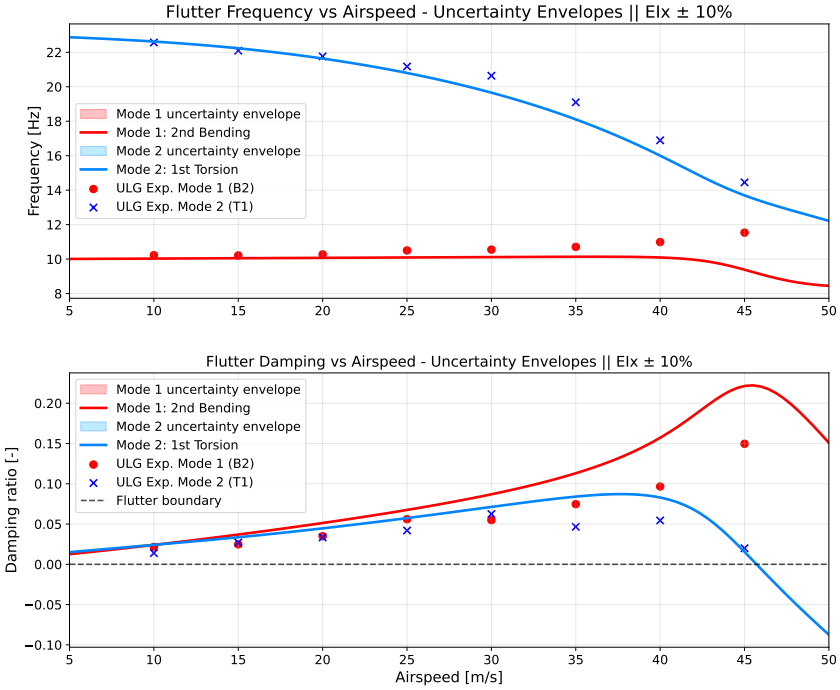

Figure 3.16: Effect of flapwise bending stiffness (EI_x = nominal $\pm$ 10%). Primary impact on bending-dominant frequency and its damping evolution.

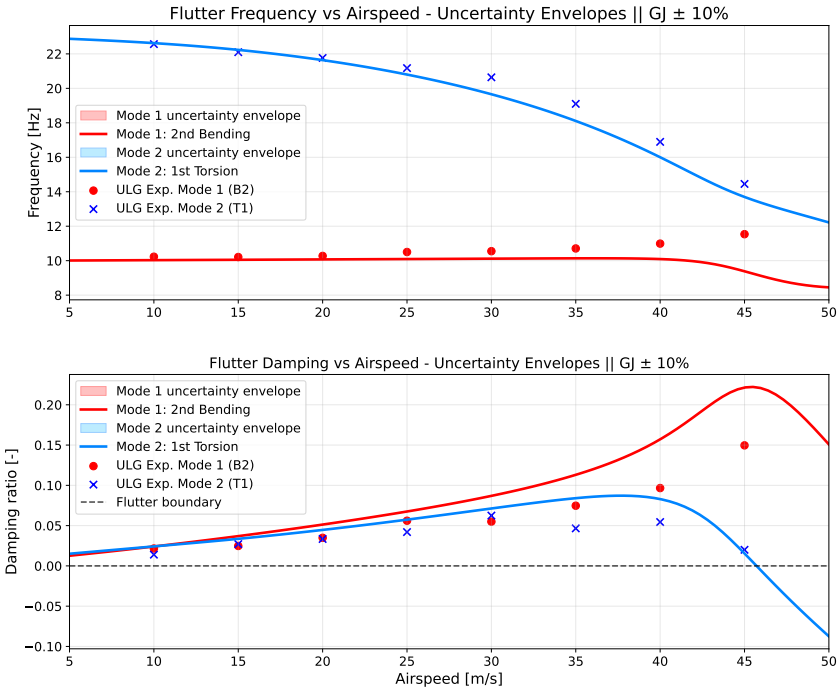

Figure 3.17: Effect of torsional stiffness (GJ = nominal $\pm$ 10%). Primary impact on torsion branch and bending-torsion proximity, increased GJ typically stabilises the system.

Damping targets: ζ_1 and ζ_α

Finally, Figure 3.18 shows the isolated effect of varying the Rayleigh targets (ζ_1, ζ_α) within $\pm 0.2\%$ around the nominal (first bending and first torsion). As expected for proportional damping, the frequency curves are practically unchanged, while the damping ratio shifts nearly rigidly. This provides a straightforward parameter to align the low-speed decay rates with measurements without compromising the frequency placement.

Across the investigated one-at-a-time uncertainty **envelopes**, the following key findings were made :

- **Aerodynamic Inputs**:
  Variations in aerodynamic parameters, most notably Mach number (M), primarily influence the damping trends by altering the unsteady aerodynamic forces. This shifts the damping curves without significantly affecting the frequency placement, as the structural stiffness and mass remain unchanged.
- **Structural Inputs**:
  Structural inputs such as mass per unit span (m), flapwise stiffness (EI_x), and torsional stiffness (GJ) are the main drivers of the frequency placement (χ) and, by extension, the degree of bending-torsion coupling. Changes in these properties directly modify the natural frequencies, leading to a wider frequency envelope.
- **Damping Inputs**:
  The Rayleigh damping targets, (ζ_1, ζ_α), have a distinct effect of primarily shifting the damping ratio. As expected from the proportional damping model, these parameters have a negligible influence on the frequency curves.

The nominal model's predictions consistently lie near the center of all uncertainty bands, and the available experimental points are well-contained within these envelopes. This consistency validates the modeling hierarchy, demonstrating that the high-fidelity cross-section reconstruction and subsequent modal analysis provide a robust and reliable foundation for aeroelastic predictions.

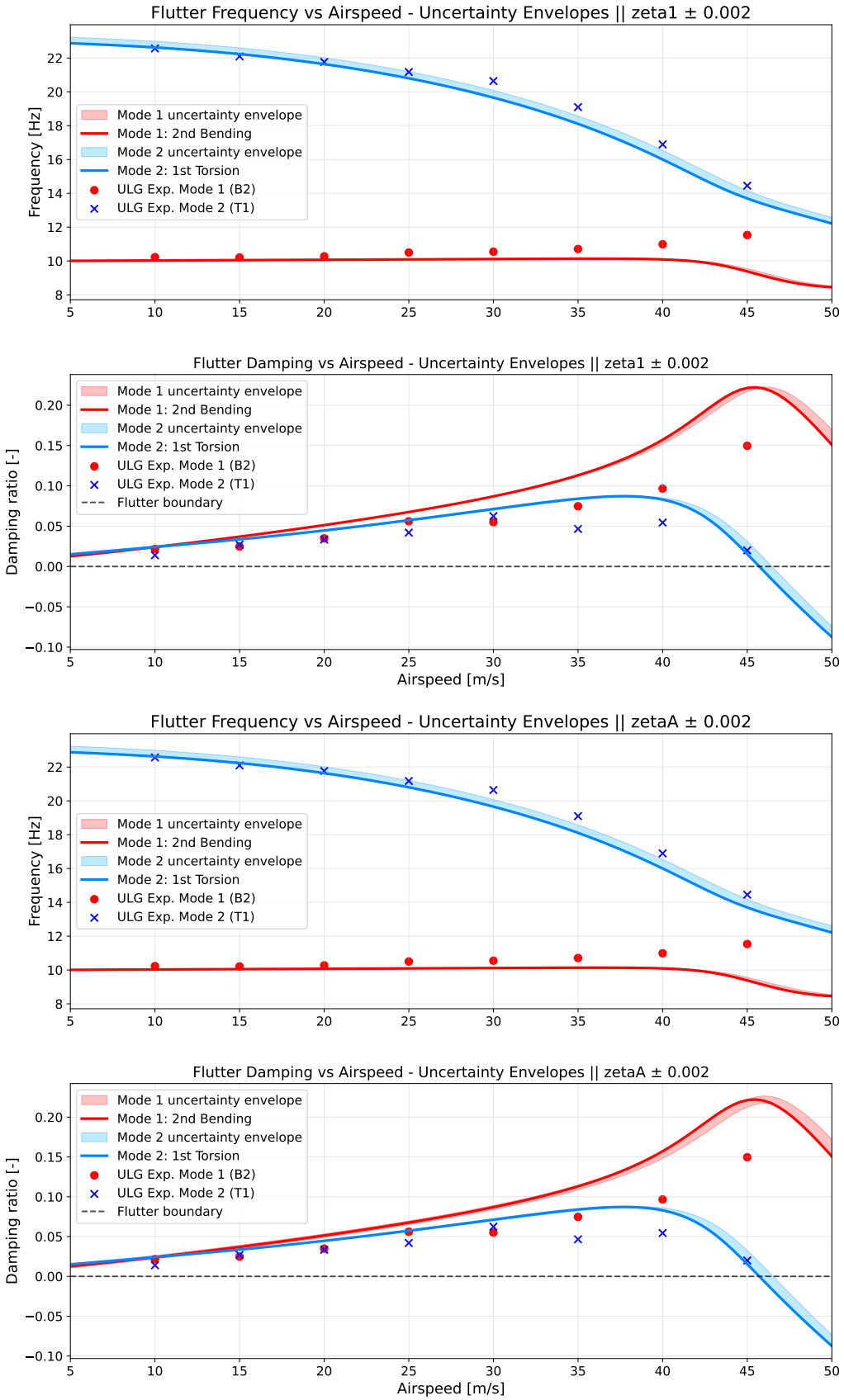

Figure 3.18: Effect of Rayleigh targets (ζ_1, ζ_α) varied by $\pm 0.2\%$. Frequencies remain effectively unchanged, damping curves shift vertically, as expected.

3.2.2 Frequency–Placement metric f_h/f_α

A convenient scalar summary of the structural–aeroelastic coupling is the **frequency placement**, defined as :

$$\chi \equiv \frac{f_h}{f_\alpha},$$

where f_h is the first bending–dominant frequency and f_α is the first torsional frequency at $U = 0$, wind-off configuration. For the nominal reconstruction, the numerical model predicts $f_h = 1.610\,\mathrm{Hz}$ and $f_\alpha = 10.065\,\mathrm{Hz}$ 3.1.3, yielding a nominal frequency placement of $\chi_{\mathrm{nom}} = 0.16$. Within the one–at–a–time bounds investigated in Section 3.2.1, χ varies over the range $[0.065,\, 0.078]$.

As it can be interpreted, a larger value of χ indicates a closer proximity of the bending and torsion modes, which leads to stronger bending–torsion coupling and, consequently, a reduced flutter margin. Conversely, smaller values of χ correspond to a greater separation of the modal branches, which is generally a stabilizing factor for the aeroelastic system.

Table 3.6: Directional influence of key parameters on the frequency placement $\chi = f_h/f_\alpha$ and on flutter susceptibility within the tested bounds. Arrows indicate the qualitative trend.

Parameter increase	**Effect on χ**	**Implication for flutter**
Mass per unit span m	$\uparrow$ (via $f_h \downarrow$)	Earlier onset / lower margin
Flapwise stiffness EI_x	$\downarrow$ (via $f_h \uparrow$)	Stabilising
Torsional stiffness GJ	$\downarrow$ (via $f_\alpha \uparrow$)	Stabilising
Aft shift of X_{cg}/c	$\uparrow$ (stronger coupling)	Earlier onset / lower margin
Mach number M	negligible on χ (frequencies rigid)	Alters damping, placement unchanged
Density ρ	negligible on χ (structural)	Scales loads, placement unchanged
Rayleigh targets (ζ_1, ζ_α)	negligible on χ	Shifts damping ratio

The uncertainty envelopes indicate that aerodynamic inputs primarily translate the damping curves with minimal impact on frequency placement, while structural inputs (m, EI_x, GJ and the X_{cg}/c - X_{sc}/c offset) govern f_h, f_α, and hence χ. As χ encapsulates the relative placement of the bending and torsional branches in a single observable quantity, targeting χ (together with the individual frequency curves) provides a concise and robust criterion for model calibration and validation prior to flutter prediction.

Chapter 4

Conclusion and Perspectives

4.1 Conclusion

A reproducible computational framework was established for linear aeroelastic stability assessment of finite wings by coupling a three-dimensional beam finite element structural model with an unsteady lifting-surface aerodynamic solver through the `SDPMflut` software. The framework assembles spanwise cross-sectional properties derived from a detailed two-dimensional analysis, constructs a reduced structural modal basis, evaluates aerodynamic generalised forces on a suitable reduced-frequency grid, and solves the coupled complex eigenvalue problem to obtain frequency– and damping– airspeed curves together with flutter metrics.

Within the scope of this thesis, the framework was verified and exercised on a ULiège wing configuration reconstructed from a high-fidelity dataset. The undamped modal characteristics reproduced the expected ordering and spatial patterns of the first bending and torsional modes. The aeroelastic trends displayed the characteristic approach and interaction of the bending and torsional branches, and the identified flutter parameters were consistent with the experimental dispersion when equivalent modelling choices and discretisation were adopted. These outcomes indicate that the beam idealisation, when informed by faithful cross-sectional properties, is sufficient to capture the governing mechanisms of classical bending–torsion flutter for the considered configuration.

Numerical reliability was addressed through two complementary routes. A discretisation study demonstrated insensitivity of the aeroelastic indicators to further refinement beyond selected structural and aerodynamic resolutions, which were then retained for production calculations. In addition, a parameter-wise uncertainty analysis quantified the effect of plausible variations in aerodynamic inputs (density, Mach number, panelling) and structural inputs (mass, bending and torsional rigidities, chordwise centre-of-gravity location). The envelopes confirmed that frequency placement is primarily controlled by structural properties, whereas aerodynamic inputs chiefly modulate damping levels. The dimensionless metric $\chi = f_h/f_\alpha$ proved useful to track how changes in stiffness and mass shift the relative position of the first bending and torsional

branches and, consequently, the propensity for coalescence.

The computational aspects of the framework were engineered for traceability and ease of reuse. Cross-sectional reconstructions, spanwise property fields, modal data, aerodynamic force matrices, and post-processed aeroelastic indicators are stored with explicit metadata and units. The exchange format towards the `SDPMflut` software is automated to limit manual intervention and to avoid configuration drift. The resulting structure provides a transparent path from geometry and material definitions to flutter identification and uncertainty envelopes.

Certain limitations must be acknowledged. The analysis is linear and time-harmonic, and structural behaviour is represented by a beam model without shell- or plate-level detail, which may under-resolve highly local bending–torsion coupling near geometric discontinuities. Structural damping was represented through Rayleigh targets rather than identified from measured decay, and aerodynamic modelling followed a lifting-surface approach that is not intended for transonic regimes or separated flows. These assumptions were appropriate for the configuration and conditions considered, but they delimit the domain of applicability.

Overall, the objectives defined in the scope of this thesis were achieved: a verified structural beam module informed by cross-sectional analysis, a consistent interface to the `SDPMflut` software for unsteady aerodynamics, a demonstrably converged flutter solution procedure, and a set of uncertainty envelopes that explain the relative influence of aerodynamic and structural inputs on stability indicators.

4.2 Perspectives

The following extensions are considered the most impactful :

Model fidelity

Adoption of measured mass distributions and inertial properties would reduce epistemic uncertainty in frequency placement. For configurations with pronounced local coupling, a hybrid strategy combining a beam backbone with local shell sub-models could be introduced to capture torsional warping near cut-outs and joints.

Aerodynamic enhancements

Alternative unsteady aerodynamic formulations and compressibility corrections could be assessed to extend the validity range. Automated selection of the reduced-frequency sampling

and of chordwise/spanwise panelling based on a posteriori indicators would deliver mesh-independent predictions at lower cost.

Identification and uncertainty

Replacing envelope analyses by probabilistic propagation with statistically characterised inputs would provide risk-aware confidence intervals on flutter metrics. Gradient-free global sensitivity measures could be used to prioritise the most influential parameters for calibration.

Automation and quality control

Rule-based checks on units, coordinate conventions, and property continuity can be integrated into the preprocessing. Adaptive modal truncation strategies that monitor contribution to the aeroelastic response would ensure efficiency without compromising accuracy.

Scope extension

Application to additional wing configurations and to manoeuvre or gust-response problems would broaden relevance. Coupling with control-law synthesis for flutter suppression is a natural next step once the prediction loop is robust and automated.

Appendix A

A.1 Element mass and stiffness matrices in local coordinates

Notation and degrees of freedom

The local element axis is x (from node 1 to node 2), with y and z forming a right-handed triad. The element length is L. Material and sectional properties are: Young's modulus E, shear modulus G, area A, torsional constant J, second moments of area I_y and I_z, mass density ρ, and shear-correction factors κ_y and κ_z. The per-node local degrees of freedom are ordered as :

$$\{q_e\}^\top = \big[\, u_1,\ v_1,\ w_1,\ \theta_{x1},\ \theta_{y1},\ \theta_{z1} \ \mid\ u_2,\ v_2,\ w_2,\ \theta_{x2},\ \theta_{y2},\ \theta_{z2} \big].$$

For compactness, the final 12×12 matrices are assembled by placing axial, torsional, and bending sub-matrices at the corresponding DOF positions.

A.1.1 Euler–Bernoulli beam element (EB)

The Euler–Bernoulli formulation neglects shear deformation. The local stiffness matrix is composed of axial, torsional, and two uncoupled bending sub-blocks.

Axial stiffness (place on DOFs u_1, u_2).

$$\mathbf{K}_{\text{ax}}^{\text{EB}} = \frac{EA}{L} \begin{bmatrix} 1 & -1 \\ -1 & 1 \end{bmatrix}.$$

Torsional stiffness (place on DOFs θ_{x1}, θ_{x2}).

$$\mathbf{K}_{\text{tor}}^{\text{EB}} = \frac{GJ}{L} \begin{bmatrix} 1 & -1 \\ -1 & 1 \end{bmatrix}.$$

Bending about z (plane x–y): acts on $[\,v_1,\ \theta_{z1},\ v_2,\ \theta_{z2}\,]$.

$$\mathbf{K}^{\mathsf{EB}}_{v\theta_z} \;=\; \frac{EI_z}{L^3}\begin{bmatrix} 12 & 6L & -12 & 6L \\ 6L & 4L^2 & -6L & 2L^2 \\ -12 & -6L & 12 & -6L \\ 6L & 2L^2 & -6L & 4L^2 \end{bmatrix}.$$

Bending about y (plane x–z): acts on $[\,w_1,\ \theta_{y1},\ w_2,\ \theta_{y2}\,]$.

$$\mathbf{K}^{\mathsf{EB}}_{w\theta_y} \;=\; \frac{EI_y}{L^3}\begin{bmatrix} 12 & 6L & -12 & 6L \\ 6L & 4L^2 & -6L & 2L^2 \\ -12 & -6L & 12 & -6L \\ 6L & 2L^2 & -6L & 4L^2 \end{bmatrix}.$$

Assembly. The 12×12 stiffness matrix $\mathbf{K}^{\mathsf{EB}}_e$ is obtained by superposing the four sub-blocks at the corresponding DOFs:

$$\mathbf{K}^{\mathsf{EB}}_e \;=\; \mathsf{place}(\mathbf{K}^{\mathsf{EB}}_{\mathsf{ax}} \text{ on } \{u_1, u_2\}) + \mathsf{place}(\mathbf{K}^{\mathsf{EB}}_{\mathsf{tor}} \text{ on } \{\theta_{x1}, \theta_{x2}\}) + \mathsf{place}(\mathbf{K}^{\mathsf{EB}}_{v\theta_z} \text{ on } \{v_1, \theta_{z1}, v_2, \theta_{z2}\}) + \mathsf{place}(\mathbf{K}^{\mathsf{EB}}_{w\theta_y}$$

Consistent mass (translational) for EB. For EB the kinetic energy depends on the translational velocity field only. The standard consistent mass blocks are:

- **Axial DOFs** (u_1, u_2):

$$\mathbf{M}^{\mathsf{EB}}_{\mathsf{ax}} = \frac{\rho AL}{6}\begin{bmatrix} 2 & 1 \\ 1 & 2 \end{bmatrix}.$$

- **Bending about** z on $[\,v_1, \theta_{z1}, v_2, \theta_{z2}\,]$:

$$\mathbf{M}^{\mathsf{EB}}_{v\theta_z} = \frac{\rho AL}{420}\begin{bmatrix} 156 & 22L & 54 & -13L \\ 22L & 4L^2 & 13L & -3L^2 \\ 54 & 13L & 156 & -22L \\ -13L & -3L^2 & -22L & 4L^2 \end{bmatrix}.$$

- **Bending about** y on $[\,w_1, \theta_{y1}, w_2, \theta_{y2}\,]$:

$$\mathbf{M}^{\mathsf{EB}}_{w\theta_y} = \frac{\rho AL}{420}\begin{bmatrix} 156 & 22L & 54 & -13L \\ 22L & 4L^2 & 13L & -3L^2 \\ 54 & 13L & 156 & -22L \\ -13L & -3L^2 & -22L & 4L^2 \end{bmatrix}.$$

- **Pure torsion** $(\theta_{x1}, \theta_{x2})$ is not activated in EB by translational inertia. If desired, a polar rotary inertia about x can be added as a separate block (see Timoshenko below).

The 12×12 mass matrix $\mathbf{M}^{\mathsf{EB}}_e$ is assembled by placing these blocks at the corresponding DOFs.

A.1.2 Timoshenko beam element (TBT)

The Timoshenko formulation accounts for shear deformation and rotary inertia. Define the dimensionless shear parameters :

$$\phi_y = \frac{12EI_z}{\kappa_y GAL^2}, \qquad \phi_z = \frac{12EI_y}{\kappa_z GAL^2}.$$

Axial and torsional stiffness.

$$\mathbf{K}_{\text{ax}}^{\text{TBT}} = \frac{EA}{L}\begin{bmatrix} 1 & -1 \\ -1 & 1 \end{bmatrix}, \qquad \mathbf{K}_{\text{tor}}^{\text{TBT}} = \frac{GJ}{L}\begin{bmatrix} 1 & -1 \\ -1 & 1 \end{bmatrix}.$$

Bending about z (plane x–y): acts on $[\, v_1, \theta_{z1}, v_2, \theta_{z2}\,]$.

$$\mathbf{K}_{v\theta_z}^{\text{TBT}} = \frac{EI_z}{L^3}\begin{bmatrix} \dfrac{12}{1+\phi_y} & \dfrac{6L}{1+\phi_y} & -\dfrac{12}{1+\phi_y} & \dfrac{6L}{1+\phi_y} \\ \dfrac{6L}{1+\phi_y} & \dfrac{(4+\phi_y)L^2}{1+\phi_y} & -\dfrac{6L}{1+\phi_y} & \dfrac{(2-\phi_y)L^2}{1+\phi_y} \\ -\dfrac{12}{1+\phi_y} & -\dfrac{6L}{1+\phi_y} & \dfrac{12}{1+\phi_y} & -\dfrac{6L}{1+\phi_y} \\ \dfrac{6L}{1+\phi_y} & \dfrac{(2-\phi_y)L^2}{1+\phi_y} & -\dfrac{6L}{1+\phi_y} & \dfrac{(4+\phi_y)L^2}{1+\phi_y} \end{bmatrix}.$$

Bending about y (plane x–z): acts on $[\, w_1, \theta_{y1}, w_2, \theta_{y2}\,]$.

$$\mathbf{K}_{w\theta_y}^{\text{TBT}} = \frac{EI_y}{L^3}\begin{bmatrix} \dfrac{12}{1+\phi_z} & \dfrac{6L}{1+\phi_z} & -\dfrac{12}{1+\phi_z} & \dfrac{6L}{1+\phi_z} \\ \dfrac{6L}{1+\phi_z} & \dfrac{(4+\phi_z)L^2}{1+\phi_z} & -\dfrac{6L}{1+\phi_z} & \dfrac{(2-\phi_z)L^2}{1+\phi_z} \\ -\dfrac{12}{1+\phi_z} & -\dfrac{6L}{1+\phi_z} & \dfrac{12}{1+\phi_z} & -\dfrac{6L}{1+\phi_z} \\ \dfrac{6L}{1+\phi_z} & \dfrac{(2-\phi_z)L^2}{1+\phi_z} & -\dfrac{6L}{1+\phi_z} & \dfrac{(4+\phi_z)L^2}{1+\phi_z} \end{bmatrix}.$$

Assembly.

$$\mathbf{K}_e^{\text{TBT}} = \text{place}(\mathbf{K}_{\text{ax}}^{\text{TBT}} \text{ on } \{u_1, u_2\}) + \text{place}(\mathbf{K}_{\text{tor}}^{\text{TBT}} \text{ on } \{\theta_{x1}, \theta_{x2}\}) + \text{place}(\mathbf{K}_{v\theta_z}^{\text{TBT}} \text{ on } \{v_1, \theta_{z1}, v_2, \theta_{z2}\}) + \text{place}(\mathbf{K}$$

Consistent mass for TBT (with rotary inertia). The kinetic energy includes translational and cross-sectional rotary contributions. The translational sub-blocks are identical to EB (given above). Rotary inertia is added as 2×2 consistent blocks on the rotational DOFs:

$$\mathbf{M}_{\theta_x}^{\text{TBT}} = \frac{\rho JL}{6}\begin{bmatrix} 2 & 1 \\ 1 & 2 \end{bmatrix}, \qquad \mathbf{M}_{\theta_y}^{\text{TBT}} = \frac{\rho I_y L}{6}\begin{bmatrix} 2 & 1 \\ 1 & 2 \end{bmatrix}, \qquad \mathbf{M}_{\theta_z}^{\text{TBT}} = \frac{\rho I_z L}{6}\begin{bmatrix} 2 & 1 \\ 1 & 2 \end{bmatrix}.$$

The full 12×12 mass matrix $\mathbf{M}_e^{\mathsf{TBT}}$ is therefore :

$$\mathbf{M}_e^{\mathsf{TBT}} \;=\; \mathbf{M}_e^{\mathsf{EB}} + \mathsf{place}\big(\mathbf{M}_{\theta_x}^{\mathsf{TBT}} \text{ on } \{\theta_{x1}, \theta_{x2}\}\big) + \mathsf{place}\big(\mathbf{M}_{\theta_y}^{\mathsf{TBT}} \text{ on } \{\theta_{y1}, \theta_{y2}\}\big) + \mathsf{place}\big(\mathbf{M}_{\theta_z}^{\mathsf{TBT}} \text{ on } \{\theta_{z1}, \theta_{z2}\}\big).$$

Remarks

- The expressions above are in the local element frame. Global matrices follow by the standard 12×12 orthogonal transformation $\mathbf{T}$ as $\mathbf{K}_e^{(g)} = \mathbf{T}^\top \mathbf{K}_e^{(\ell)} \mathbf{T}$ and $\mathbf{M}_e^{(g)} = \mathbf{T}^\top \mathbf{M}_e^{(\ell)} \mathbf{T}$.
- The parameters ϕ_y and ϕ_z embed shear flexibility via κ_y and κ_z. In the limit $\phi_y, \phi_z \to 0$, the Timoshenko bending blocks recover the Euler–Bernoulli form.
- If required, Cowper-type refinements of rotary inertia and shear corrections can be introduced by adjusting κ_y, κ_z and the rotary blocks, without altering the assembly pattern.

Bibliography

[1] T. Andrianne, *Aeroelasticity and experimental aerodynamics — course aero0032-1*, Lecture notes and course materials; academic year 2024–2025, Liège, Belgium, 2025.

[2] R. L. Bisplinghoff, H. Ashley, and R. L. Halfman, *Aeroelasticity*. New York: Dover Publications, 1983.

[3] G. Dimitriadis, *Unsteady Aerodynamics: Potential and Vortex Methods* (Aerospace Series). Hoboken: Wiley, 2024.

[4] G. Dimitriadis. "SDPMflut Software." Unsteady Source and Doublet Panel Method flutter solver. Founder: Prof. Grigorios Dimitriadis, AeroConsult. (), [Online]. Available: `https://aeroconsult.gr/sdpmflut-software/` (visited on 08/15/2025).

[5] Y.-C. Fung, *An Introduction to the Theory of Aeroelasticity*. Mineola, NY: Dover Publications, 2002, Reprint of the 1955 edition.

[6] J. Lonsain, "Aeroelastic analysis of a 3d wing structure with a flexible trailing edge," M.S. thesis, Delft University of Technology, Delft, The Netherlands, Mar. 2017.

[7] M. Pirnay, "Aeroelastic analysis of a slender wing: Wind tunnel tests and modelling," Academic year 2024–2025, Master's thesis, University of Liège, Liège, Belgium, 2025.

[8] B. Prieur, "Contrôle piézoélectrique des charges et instabilités aéroélastiques sur aile flexible," École polytechnique, Rapport de stage de recherche, 2023, Encadré au CNAM (LMSSC) par Xavier Amandolese et Boris Lossouarn.

[9] L. Salles, *Theory of vibration — course meca0029-1*, Lecture notes and course materials; academic year 2024–2025, Liège, Belgium, 2025.

[10] L. Salles, *Vibration testing and experimental modal analysis — course meca0062-1*, Lecture notes and course materials; academic year 2024–2025, Liège, Belgium, 2025.